Cristofani Riccardo (Orcid ID: 0000-0003-2719-846X)
Poletti Angelo (Orcid ID: 0000-0002-8883-0468)

Pathogenic variants of Valosin Containing Protein induce lysosomal damage and transcriptional activation of autophagy regulators in neuronal cells

Veronica Ferrari[1], Riccardo Cristofani[1], Maria E. Cicardi[2], Barbara Tedesco [1,3] Valeria Crippa[1], Marta Chierichetti[1], Elena Casarotto[1], Marta Cozzi[1], Francesco Mina[1], Mariarita Galbiati[1], Margherita Piccolella[1], Serena Carra[4], Thomas Vaccari[5], Angele Nalbandian[6], Virginia Kimonis[6], Tyler R. Fortuna[7], Udai B. Pandey[7,8], Maria C. Gagliani[9], Katia Cortese[9]*, Paola Rusmini[1], Angelo Poletti[1]*

[1] *Dipartimento di Scienze Farmacologiche e Biomolecolari, Centre of Excellence on Neurodegenerative Diseases, Università degli Studi di Milano, Milan, MI, Italy.*

[2] *Department of Neuroscience, Weinberg ALS Center, Vickie and Jack Farber Institute for Neuroscience, Thomas Jefferson University, Philadelphia, PA, USA.*

[3] *Unit of Medical Genetics and Neurogenetics, Fondazione IRCCS – Istituto Neurologico "Carlo Besta", Milan, MI, Italy.*

[4] *Department of Biomedical, Metabolic and Neural Sciences, University of Modena and Reggio Emilia, Modena, MO, Italy.*

[5] *Dipartimento di Bioscienze, Università degli Studi di Milano, Milan, MI, Italy.*

[6] *Department of Pediatrics, University of California, Irvine, CA, USA.*

[7] *Department of Pediatrics, Children's Hospital of Pittsburgh, University of Pittsburgh Medical Center, Pittsburgh, PA, USA.*

[8] *Department of Human Genetics, Graduate School of Public Health, University of Pittsburgh, Pittsburgh, PA, USA.*

[9]*Department of Experimental Medicine (DIMES), Cellular Electron Microscopy Lab, University of Genoa, Genova (Genova), Italy.*

This article has been accepted for publication and undergone full peer review but has not been through the copyediting, typesetting, pagination and proofreading process which may lead to differences between this version and the Version of Record. Please cite this article as doi: 10.1002/nan.12818

* *Co-corresponding Authors*

Angelo Poletti, Dipartimento di Scienze Farmacologiche e Biomolecolari, via Balzaretti 9, 20133 Milano (Italy), e-mail: angelo.poletti@unimi.it

Katia Cortese, Department of Experimental Medicine, University of Genoa, Via Antonio de Toni 14, 16132 Genova (Italy), e-mail: cortesek@unige.it

Keywords: ALS; lysosome; neurodegeneration; TFE3; p97; PQC

Running title: Valosin Containing Protein variants induce lysosomal damage and autophagy

Key points:

- VCP mutants trigger lysosomal damage and morphological alterations, with increased size, decreased acidification, and impaired enzyme activity.
- VCP mutants enhance autophagic flux in a specific TFE3-dependent mechanism.
- VCP wt modulation decreases levels of chemically and biologically induced lysosomal damage.
- VCP wt and mutants decrease the insoluble levels of SOD1 mutant.

Words of the main body: **6167**

Number of figures: 8

Abstract

Aim: Mutations in the Valosin-containing protein (*VCP*) gene cause various lethal proteinopathies that mainly include inclusion body myopathy with Paget's disease of bone frontotemporal dementia (IBMPFD) and amyotrophic lateral sclerosis (ALS). Different pathological mechanisms have been proposed. Here, we define the impact of VCP mutants on lysosomes and how cellular homeostasis is restored by inducing autophagy in the presence of lysosomal damage.

Methods: By electron microscopy, we studied lysosomal morphology in VCP animal and motoneuronal models. Using western blotting, RT-qPCR, immunofluorescence, and filter trap assay, we evaluated the effect of selected VCP mutants in neuronal cells on lysosome size and activity, lysosomal membrane permeabilization, and their impact on autophagy.

Results: We found that VCP mutants induced aberrant multilamellar organelles in VCP animal and cell models similar to those found in patients with *VCP* mutations or with lysosomal storage disorders. In neuronal cells, we found altered lysosomal activity characterized by membrane permeabilization with galectin-3 redistribution and activation of PPP3CB. This selectively activated the autophagy/lysosomal transcriptional regulator TFE3, but not TFEB, and enhanced both SQSTM1/p62 and lipidated MAP1LC3B levels inducing autophagy. Moreover, we found that WT VCP, but not the mutants, counteracted lysosomal damage induced either by trehalose or by a mutant form of SOD1 (G93A), also blocking the formation of its insoluble intracellular aggregates. Thus, chronic activation of autophagy might fuel the formation of multilamellar bodies.

Conclusion: Together, our findings provide insights into the pathogenesis of VCP-related diseases, by proposing a novel mechanism of multilamellar body formation induced by VCP mutants that involves lysosomal damage and induction of lysophagy.

Abbreviations

AAA^+: ATPases associated with diverse cellular activities; ALS: amyotrophic lateral sclerosis; CLEAR: coordinated lysosomal expression and regulation; DAPI: 4′,6-diamidino-2-phenylindole; DMEM: Dulbecco's modified Eagle's medium; EGFP: enhanced green fluorescent protein; EM: electron microscopy; ER: endoplasmic reticulum; fALS: familial amyotrophic lateral sclerosis; FTA: filter trap assay; FTD: frontotemporal dementia; GAPDH: glyceraldehyde-3-phosphate dehydrogenase; IBMPFD: inclusion body myopathy with early-

onset Paget disease and frontotemporal dementia; IF: immunofluorescence analysis; LAMP1: lysosomal-associated membrane protein 1; LGALS3: lectin, galactose binding, soluble 3; LLOMe: L-leucyl-L-leucine methyl ester; LMP: lysosomal membrane permeabilization; Lys: lysosomes; MAP1LC3B: microtubule-associated protein 1 light chain 3 beta; MLBs: multilamellar bodies; MSP: multisystem proteinopathy; NPL4: nuclear protein localization protein 4; NSC-34: neuroblastoma spinal cord 34; PBS: phosphate-buffered saline; PLAA: Phospholipase A2 activating protein; PQC: protein quality control; PPP3CB: protein phosphatase 3, catalytic subunit, beta isoform; SD: standard deviation; siRNA: small interfering RNA; SOD1: superoxide dismutase 1; SQSTM1/p62: sequestosome 1; STED: stimulated emission depletion; TARDBP/TDP-43: TAR DNA binding protein-43; TFE3: transcription factor binding to IGHM enhancer 3; TFEB: transcription factor EB; WB: western blotting; UBXD1: UBX domain-containing 1; UPS: ubiquitin proteasome system; VCP: Valosin containing protein; WT: Wild type.

Introduction

Valosin containing protein (VCP) is a ubiquitously expressed ATPase associated with diverse cellular activities (AAA^+) (1,2), which is critical in cellular homeostasis. VCP contains two ATPase domains, the D1 site energizes VCP homohexamer formation, while the D2 site supports VCP biological functions (3). VCP N- and C-terminals interact with adaptors and cofactors (4). VCP is mainly a soluble cytoplasmic protein, but partly associates with the membranes of several organelles (e.g., the endoplasmic reticulum (ER), Golgi apparatus, mitochondria, and some endosomes and lysosomes) or localizes to the nucleus (5–9). Nuclear VCP is involved in protein quality control (PQC) and chromatin remodelling processes (10–12), while cytoplasmic VCP participates in unfolded protein degradation, and in organelle formation and degradation. VCP substrate recognition is mediated by cofactors (e.g., UBX domain-containing 1 (UBXD1), Phospholipase A2 activating protein (PLAA), and UFD1-

NPL4 complex) that mark substrates (i.e., misfolded proteins), leading to their ubiquitination or deubiquitination and subsequent VCP-mediated segregation from membranes, macromolecular complexes, or protein aggregates for ubiquitin proteasome system (UPS) degradation (13–15). VCP also controls damaged DNA repair (16), regulates damaged lysosomes and mitochondria degradation (9,17), and cooperates in autophagy (18,19).

VCP mutations cause inclusion body myopathy with early-onset Paget disease and frontotemporal dementia (IBMPFD), also known as multisystem proteinopathies (MSP), familial forms of amyotrophic lateral sclerosis (fALS), and/or frontotemporal dementia (FTD) and Parkinson's disease (20-23). MSPs are age-related degenerative diseases involving muscle, bone, and brain that are associated with *VCP* mutations, and other genes that are less common (23–26). The *VCP* variants alter ATP binding, thus modifying VCP conformation and binding with some cofactors (27–29). This perturbs the PQC system, altering the handling and clearance of misfolded proteins, and the clearance of damaged organelles (16,30–33). Indeed, VCP mutants cause TAR-DNA binding protein-43 (TARDBP/TDP-43) mislocalization and aggregation, typical findings in sporadic ALS (sALS) and FTD (21).

Wild type (WT) and mutant VCP affect autophagy, but their role in this process is still debated. VCP regulates the lipid phosphatidylinositol-3-phosphate (PtdIns3P) via beclin1 (BECN1)-containing phosphatidylinositol 3-kinase (PtdIns3K) complex and ataxin 3 (ATXN3) deubiquitinase activity, which stabilizes BECN1 promoting PtdIns3K complex formation and activity. VCP also promotes biogenesis of autophagosomes, and its inhibition alters initiation of autophagy (34). Both *VCP* silencing and pathogenic *VCP* variants lead to impairment of autophagy with an accumulation of sequestosome-1 (SQSTM1/p62) and the activated form of microtubule-associated proteins 1A/1B light chain 3B (MAP1LC3B) (35,36). However, some reports have pointed to the opposite effect of VCP in autophagy: the inhibition of VCP is associated with SQSTM1/p62 degradation that is reversed by blocking autophagy (19). Despite

this, it is well established that VCP-regulated autophagy is essential for lysosomal dynamics and damaged lysosomal clearance (lysophagy). In cooperation with specific cofactors (PLAA, UBXD1, YOD1 deubiquitinase), VCP assists galectin-3 (LGALS3) activity in the removal of damaged lysosomes. VCP selectively removes K48-ubiquitinated substrates from a subset of damaged lysosomes promoting their clearance. This activity is lost by VCP mutants (9). Moreover, *Vcp* knockout in mouse muscles induces a necrotic myopathy with damaged lysosomes and LGALS3 upregulation, inducing autophagy via transcription factor EB (TFEB) activation (37). TFEB is activated by treatment with L-leucyl-L-leucine methyl ester (LLOMe), which induces lysosomal membrane permeabilization (LMP). After a recovery phase, LLOMe-activated TFEB remains localized in the nucleus when *VCP* is inactivated or VCP mutants are expressed. This suggests that WT and mutant VCP modulate TFEB activity. Notably, lysosomal damage with LGALS3 and LAMP1-positive puncta and TFEB activation is detectable in muscles of the VCP-disease mouse model. However, in this model, TFEB redistribution occurs only at very late stages of disease (one-year-old mice), suggesting that TFEB does not play a direct role in the early stages of the disease.

Therefore, it is established that WT VCP and its mutants have different effects on the recovery from induced lysosomal damage. Nevertheless, it is still unclear whether VCP mutants directly induce lysosomal damage in basal conditions, or what mechanisms activate lysophagy in the early stages of the disease.

Here, we studied whether VCP mutants linked to fALS/FTD impact lysosomal functions and whether this results in the modulation of basal autophagy in affected motoneurons. We found that VCP mutants directly affect lysosomal dynamics and specifically impact autophagic activity via the activation of transcription factor binding to IGHM enhancer 3 (TFE3), but not activation of TFEB. TFE3 activation is induced by dephosphorylation via protein phosphatase 3 catalytic subunit beta (PPP3CB). Its activation enhances SQSTM1/p62 levels and

MAP1LC3B lipidation, with potentiation of autophagic flux. This enhances lysophagy, clearing damaged lysosomes in response to mutant VCP expression. We also found that WT VCP, but not mutant VCPs, counteract lysosomal damage induced either by trehalose or by mutant G93A SOD1, preventing intracellular aggregate formation.

Protective and detrimental activities were linked to the intracellular response to mutant VCP expression, eventually dysregulating the response of the PQC system.

Materials and Methods

Chemicals

The following chemicals were used; D-(+)-trehalose dihydrate(trehalose) (100mM, Sigma-Aldrich, T9531); NH_4Cl (4mM, Euroclone, EMRO895009); Chloroquine/CQ (25μM, Sigma-Aldrich, C6628).

Plasmids and siRNAs

pFLAG-VCP WT and pFLAG-VCP R155H encoding for human WT VCP and R155H mutant were obtained from Prof. J.P. Taylor (Cell & Molecular Biology Department, St. Jude Children's Research Hospital, Memphis, TN, USA). pFLAG-VCP R191Q was obtained by single-nucleotide mutagenesis from pFLAG-VCP WT (Eurofins Genomics), replacing guanine with adenosine to convert the Arginine 191 into Glutamine.

p6xHIS-VCP WT, p6xHIS-VCP R155H, and p6xHIS-VCP R191Q were obtained by excising the FLAG tag from pFLAG-VCPs with HindIII/EsprI and inserting an in frame a 6xHIS sequence.

pEGFP-LGALS3 is from Prof. M. A. Jäättelä (Danish Cancer Society Research Center, Copenhagen, Denmark).

pEGFP-N1-TFEB and pEGFP-N1-TFE3 were obtained from Prof. Shawn Ferguson (Addgene plasmids #38119 and #38120, respectively; http://n2t.net/addgene:38120; RRID: Addgene_38120; http://n2t.net/addgene:38119; RRID: Addgene_38119 (38)).

pLAMP1-GFP was obtained from Prof. Ron Vale (Addgene plasmid #16290; http://n2t.net/addgene:16290; RRID: Addgene_16290 (2)).

pSOD1 WT and pSOD1 G93A were obtained from Dr Caterina Bendotti (Mario Negri Institute, Milano, Italy).

pCDNA3 is from Life Technologies (V790-20), and pEGFPN1 from Clontech (U55762).

The following siRNA duplex was used for silencing mPPP3CB expression: siRNA sense: 5′UGACAGAAAUGUUGGUAAAUU3′ and antisense: 5′UUUACCAA CAUUUCUGUCAUU3’ (Dharmacon); the non-targeting siRNA sense: 5′UAGCGACUAAACACAUCAAUU3′ and antisense: 5′UUGA UGUGUUUAGUCGCUAUU3′ (Dharmacon).

Cell cultures and transfections

Neuroblastoma spinal cord (NSC-34) cells are mouse motoneuron immortalized cells routinely used in our laboratory. NSC-34 cells were maintained as described (39), and plated as follows: for RT-qPCR, WB, FTA, lysosomal activity test and lysosomal acidification status in 12-well plates at 90,000cells/ml; for IF, STED, Galectin puncta assay and lysosomal size and number analysis on 13-mm coverslips in 24-well plates at 70,000cells/ml. Plasmids were transfected for 48hrs using Lipofectamine3000® Transfection Reagent (Invitrogen, ThermoFisher-Scientific, L3000-015) following the manufacturer’s protocol.

siRNAs were transfected for 72hrs using Lipofectamine2000 (Life-Technologies, 11668019) with 40pmol in 12-well plates and 20pmol in 24-well plates, following the manufacturer’s protocol.

Animals

Transgenic R155H VCP mice were generated on 129/SvEv (40) and backcrossed more than 6 times with the C57BL/6 strain so that the majority (>98%) of the genetic background of the generated mice was of C57BL/6 origin. Littermates were used for experiments and maintained as previously described (40).

For conditional ubiquitous expression in *Drosophila*, UAS-VCP (WT and mutant R152H) lines (41) were crossed with the inducible driver, TubGS-Gal4. Day 1 adults from the F1 progeny were collected every 24hrs and moved to standard media mixed with 20mM RU486 as described (42,43). The F1 progeny adults were aged for 10 days at 25°C when the thorax was dissected out and fixed in Davidson's fixative (Electron Microscopy Sciences; #64133-10).

Real-time quantitative polymerase chain reaction (RT- qPCR)

NSC-34 cells were transfected with target siRNA or with plasmid listed in Supporting information-Table 2. Total RNA was extracted using Tri-Reagent (Sigma-Aldrich, T9424) following the manufacturer's protocol. Before reverse transcription (RT) of RNA samples, the RNA concentration and quality were tested measuring the ratio of the absorbance at 260nm/280nm and 260nm/230nm for each sample (data are included in Supporting information-Table 3, 4). 1µg per sample was treated with DNase and reverse transcribed using the High-Capacity cDNA Reverse Transcription Kit (ThermoFisher-Scientific, 4368814).

RT-qPCR was performed using the CFX96 Real-Time System (Bio-Rad Laboratories), the iTaq SYBR Green Supermix (Bio-Rad Laboratories, 1725124), and with a final concentration of 500nM of primers. Data were normalized using Rplp0. The experiments were performed with 4 independent samples (n=4).

Western blotting (WB) and filter trap assay (FTA)

NSC-34 were transfected with plasmid listed in Supporting information-Table 2.

Cells were harvested, centrifuged, resuspended, and lysed as described (44). Total protein content was quantified with bicinchoninic acid (BCA) assay (Cyanagen, PRTD1).

For WB analysis, 15μg protein/samples added with β-mercaptoethanol and SDS to denature and linearize proteins, were loaded on a polyacrylamide gel. After electrophoresis, proteins were transferred with Trans-Blot Turbo (Bio-Rad Laboratories, 1704150) for 40min at 25V at RT on a 0.45μm nitrocellulose membrane (Bio-Rad Laboratories, 1620115).

For FTA, 6μg protein/samples were filtered on a 0.22μm cellulose-acetate membrane (Whatman, 100404180) using a Bio-Dot SF Microfiltration Apparatus (Bio-Rad Laboratories, 1703938). Then proteins were fixed with 20% methanol solution.

To quantify cytoplasmic and nuclear levels of TFEB and TFE3, NSC-34 cells were plated in 6-well plates at 90,000cells/ml and transfected with plasmids listed in Supporting information-Table 2, or treated for 24hrs with trehalose. Cells were harvested, centrifuged, and lysed and nuclear-cytoplasmic fractions were isolated as described (44,45). Antibodies used for WB assay and FTA are listed in Supporting information-Table 1. Immunoreactivity was detected with enhanced chemiluminescent (ECL) detection reagent (Westar Antares, Cyanagen XLS0142) acquiring images with Chemidoc XRS System (Bio-Rad Laboratories, 1708265). Densitometric quantification was performed using Image Lab Software, version5.2.1 (Bio-Rad Laboratories).

Immunofluorescence (IF) analysis

NSC-34 were transfected with plasmids listed in Supporting information-Table 2. To induce chemical lysosome damage, cells were treated with trehalose for 2, 6, or 18hrs. Cells were fixed with 4% paraformaldehyde solution, permeabilized for 15min using 10% Triton X-100 in PBS solution, incubated for 1hr at RT in blocking solution and then with primary antibody overnight at 4°C followed by 1hr at RT with secondary antibody. Nuclei were stained with DAPI

(1:10,000 in PBS). Coverslips were mounted using Mowiol® 4-88 (Merck-Millipore, 475904). Images were acquired with Axiovert 200 microscope (Zeiss, Oberkochen, Germany). TFEB and TFE3 nuclear intensities were quantified with ImageJ software as described (44). The size of SQSTM1/p62 and MAP1LC3B puncta of aggregate-like structures and their cellular distribution at single-cell resolution were quantified using an ImageJ macro (AggreCount(46)) for unbiased analyses of cellular aggregate-like structures. Antibodies used for IF assay, are found listed in Supporting information-Table 1. To quantify lysosomal number and size, images were acquired with LSM510 Meta system confocal microscope (Zeiss) and were processed with the Aim 4.2 software (Zeiss). Z-stacks of 11 randomly selected fields per condition (see Fig. legends for details) were acquired, and lysosomal number and volume were quantified with Arivis Vision4D software.

Stimulated emission depletion (STED) microscopy

NSC-34 were transfected with plasmids listed in Supporting information-Table 2. Cells were fixed, permeabilized and processed as described for IF assay. Images were taken with a Leica TCS SP8 STED 3X microscope with 3 depletion lines (592, 660 and 775nm), with HC PL APO 100X/1.40 oil objective, acquired through the Software Leica LAS X and processed using ImageJ (version 1.51).

Galectin puncta assay

NSC-34 were transfected with plasmids listed in Supporting information-Table 2. To induce chemical lysosome damage, cells were treated with trehalose for 2, 6, or 18hrs. 48hrs from transfection, cells were processed as described for IF assay. Cells with >3 EGFP-LGALS3 puncta as described in (44) were manually quantified in 3 randomly selected fields per sample (see Fig. legends for details) and 3 samples per condition using a PL 20X eyepiece with graticules (100mm×10mm in 100-grid divisions). Cells expressing GFP were counted in the

same field. The ratio between cells with >3 EGFP-LGALS3 puncta and transfected cells was calculated on each field of view and statistical analysis was performed.

Lysosomal activity

Lysosomal enzyme activity was measured by cytometer analysis in NSC-34 transfected with plasmids listed in Supporting information-Table 2. Cells were incubated in high glucose medium with 0.5% of FBS and self-quenched substrate (PromoCell, PK-CA577-K448) for 1hr as described by the manufacturer and then collected, washed twice in 1ml assay buffer, resuspended in PBS, and analyzed on a NovoCyte flow cytometer (Acea Biosciences, Inc). Mean fluorescence intensity (MFI) of the self-quenched substrate was recorded from 10,000 cells for each sample (n=6).

Lysosomal acidification status

Relative lysosomal acidification status was measured in NSC-34 transfected with plasmids listed in Supporting information-Table 2, and treated with trehalose for different time periods (from 2 to 18hrs). Next, the cells were incubated with 100nM of lysosomotropic probe LysoTracker Green DND-26 (ThermoFisher Scientific, L7526) for 30min. The cells were collected, resuspended in 4% FBS in PBS and analyzed with NovoCyte flow cytometer (Acea Biosciences, Inc.). The mean LysoTracker fluorescence intensity was recorded from 50,000 cells for each sample (n=4).

Electron microscopy (EM) analysis

NSC-34 cells were plated at 90,000 cells/ml in a 2-well Nunc®Lab-Tek®Chamber Slide™ system (Nunc, C6682) and transfected with plasmids listed in Supporting information-Table 2. Cells were then washed in 0.1M cacodylate buffer and fixed in 0.1M cacodylate buffer containing 2.5% glutaraldehyde (Electron Microscopy Science, Hatfield, PA, USA) for 1hr at RT. Cells were post-fixed in 1% osmium tetroxide for 2hrs and 1% aqueous uranyl acetate for

1hr, dehydrated through a graded ethanol series and flat embedded in resin (Poly-Bed; Polysciences, Inc., Warrington, PA) for 24hrs at 60°C. Ultrathin sections (50nm) were cut parallel to the substrate and counterstained with 5% uranyl acetate in 50% ethanol. 30 images from each sample were collected at 25,000x magnification for measurements of lysosomal diameters.

For ultrastructural analysis of animal tissues, W1118, WT VCP and mutant R152H VCP adult *Drosophila* (day10) muscle thoraces were placed in cacodylate buffer containing 2.5% glutaraldehyde for 24hrs, post-fixed in 1% osmium tetroxide and 1% uranyl acetate for 1hr each, dehydrated through a graded ethanol series and with propylene oxide for 1hr. Next, tissues were embedded in epoxy resin (Poly-Bed; Polysciences, Inc.) overnight at 42°C and 2 days at 60°C. Ultrathin sections (50nm) were observed with a HITACHI 7800 120Kv electron microscope (Hitachi, Tokyo, Japan), and digital images acquired with Megaview3 CCD camera and RADIUS software (EMSIS, Germany). Quantification of lysosome size was performed as described for NSC-34 cells. Post-processing on digital images was performed with Adobe Photoshop2021 and Adobe Illustrator2021.

For analysis of quadriceps muscle from WT and knock-in mutant VCP R155H 10-month-old mice, 3 wt control mice and 8 VCP R155H mutant littermates were fixed for 24hrs at 4°C in 0.1M PBS solution added with 4% paraformaldehyde and 0.1% glutaraldehyde. Tissue samples were fixed for 1hr at 4°C in 1% osmium solution and subsequently dehydrated in ethanol. Ultrathin (60, 80nm) sections were cut, stained, and incubated as described (47). Electron micrographs were taken with a Gatan UltraScan US1000 digital camera and analyzed for architectural differences and lipid accumulation.

Statistical analysis

The data in figure 1 are presented as median–range as they do not follow a Gaussian distribution, all the other data are presented as mean ± SD. For a variable in two groups, an

unpaired t-test was used. In the presence of 3 or more groups, one-way analysis of variance (ANOVA) was used followed by a *post hoc* test as described in the legends. An unpaired t-test with Welch's correction was used when the SDs were significantly different as determined by Bartlett's test (see figure legends for details). Statistical analysis was performed using two-way ANOVA to compare the effect of 2 independent variables when 3 or more groups were present. When two-way ANOVA was significant, a *post hoc* test was performed (see figure legends for details). P values<0.05 were considered statistically significant. All the analyses were undertaken with the PRISM (version 8.2.1.) software.

Results

VCP mutants aggregate and induce lysosomal damage.

VCP-patient muscles are characterized by degeneration and the presence of mutant VCP inclusions (48). We noted some published EM images of these skeletal muscles showing abnormal multilamellar-structures, not originally described by the authors (48), that morphologically resembled the membranous concentric bodies typically found in lysosomal storage diseases (LSD) (49,50). In LSDs, lysosomes mostly containing undegraded phospholipids and cholesterol accumulate forming multilamellar bodies (MLBs). The formation of MLBs might be a consequence of an impairment in autophagy. Indeed, initially single or multiple foci of lamellae appear within an autophagic vacuole and then transform into multilamellar structures (51). To evaluate whether these multilamellar structures are a specific feature of VCP-disease in muscle, we analyzed EM tissue samples derived from flies (*Drosophila melanogaster)* expressing WT or R152H Vcp under the control of a conditional ubiquitous driver (Tub-GS), and from mutant mice expressing the R155H Vcp. The thoracic muscles from VCP flies (Figure 1A) and quadriceps muscles from mice (Figure 1B) showed MLBs (evidenced by arrows) in large areas of the tissues. We thus investigated whether MLBs are formed only as a chronic response to the stressor activities of mutant VCP, as they are

present in the late stages of the disease, or whether they could be acutely induced in overexpressing cells. Therefore, using transient transfection, we established VCP motoneuronal cell models to analyze whether MLBs appear in EM under acute conditions. Two ALS-associated VCP mutants, R155H VCP and R191Q VCP, were expressed in the immortalized murine motoneuronal cell line NSC-34, widely used as a *bona fide* neuronal model in ALS (52–54). Figure 1C shows that cells expressing VCP mutants, particularly R155H VCP, have abnormal lysosome morphology, very similar to those seen in the muscles of the animal models (Figure 1A, B) and in skeletal muscle of VCP patients (48). MLBs in R191Q VCP/NSC-34 cells were less pronounced compared to those found in R155H VCP/NSC-34 cells. Several abnormal membranes were also retained in the lumen of these lysosomes that were not present in NSC-34 cells overexpressing WT VCP. Unfortunately, their large variability in size and form prevented us from performing quantification of these structures. Thus, we determined whether the size of lysosomes from which the MLBs are derived is increased in the presence of the mutated forms of VCP. Very interestingly, we found a robust increase of lysosomal size both in the muscle of R152H VCP flies (Figure 1 D) and in R155H VCP/NSC-34 cells (Figure 1 E), compared to their respective controls. A trend toward increased lysosome size was noted also in R191Q VCP/NSC-34 cells, but this did not reach statistical significance, suggesting that this VCP mutant is less potent at producing an acute alteration of lysosomes.

We analyzed how these acutely induced structures associate with altered lysosomal membrane conformation in response to VCP mutants. Since VCP mutants form insoluble species in skeletal muscles (20,55), we studied whether this aggregation-prone behaviour is maintained in motoneuronal cells. We overexpressed FLAG-tagged WT or mutant VCPs in motoneurons and found that both the VCP mutants are mostly present diffusely in the cytoplasm, but that there are a few small cytoplasmic FLAG-positive puncta (evidenced by the arrows) of tiny

protein aggregates (Figure 2A), not present in control cells. In WB, the anti-FLAG antibody recognized similar levels and turnover of the exogenous FLAG-tagged VCPs (Figure 2B). On the contrary, the anti-VCP antibody, which recognizes both exogenous and endogenous VCP, showed that the exogenous expression of human VCP (either WT or mutated) reduced the endogenous murine VCP levels (Figure 2B). By FTA, we further characterized the aggregation propensity of VCP mutants (Figure 2C, D) using both the anti-VCP and the anti-FLAG antibodies. Exogenous VCPs formed high molecular weight PBS-insoluble species, which were particularly elevated for R191Q VCP. Thus, these data recapitulate those of IF analyses and correlate with published data obtained in muscle cells, demonstrating that both R155H VCP and R191Q VCP form aggregates in motoneuronal cells.

Generally, protein aggregates alter different cellular pathways and the dynamics of organelles, including lysosomes (56–59). We thus studied by conventional and STED microscopy whether VCP mutants lead to alterations of lysosome dynamics, by monitoring the distribution of GFP-tagged LAMP1, a protein associated with lysosomal membranes. Notably, both VCP mutants, but not WT, induced lysosome enlargement (Figure 2E) with a filled lumen (Figure 2F, arrowheads). These morphological alterations confirmed the EM studies (Figure 1C), which also showed altered morphology and enlarged lysosomes. To determine whether aberrant lysosome structure and morphology correlate with altered lysosome function, we analyzed the activity of lysosomal enzymes. We found a decrease in lysosomal enzyme activity in cells expressing R155H VCP, but not WT VCP (Figure 2G). The possibility of LMP impairment was studied by analyzing the distribution of GFP-tagged galectin-3 (GFP-LGALS3), a small sugar-binding protein that accumulates on the lysosomal membrane only upon its permeabilization. In basal condition, GFP-LGALS3 is present diffusely in the cytoplasm and no puncta can be observed (Figure 2H); however, when lysosomal damage and LMP are induced, GFP-LGALS3 translocates and binds to the leaky lysosomes, forming puncta on the

damaged lysosomal membrane. We observed GFP-LGALS3 puncta in cells expressing VCP mutants (Figure 2H, I), but not WT VCP. The quantification of GFP-LGALS3 puncta (Figure 2J), based on a standardized procedure that considers positive cells as containing at least 3 GFP-LGALS3 puncta per cell (44), confirmed that both VCP mutants, particularly R155H VCP, significantly increased lysosomal damage compared to control VCP. Together, these results show for the first time that the acute expression of VCP mutants is sufficient to cause detrimental alterations in lysosomal stability and dynamics.

WT VCP modulation decreases damaged lysosome levels.

Upon pharmacological stress or exposure to misfolded proteins, lysophagy is activated to trigger the clearance of damaged lysosomes, however VCP mutants may compromise this process (9). We studied whether VCP mutants exerted a deleterious effect on damaged lysosomes in motoneurons. To study this issue, we chemically induced subtle lysosomal damage using trehalose, which differs from LLOMe, a known lysosomotropic agent. Trehalose induces limited, transient lysosomal damage which activates a protective autophagic response potentiating lysophagy (44). In fact, we found that LLOMe treatment is cytotoxic to motoneuronal cells, while trehalose exposure for up to 18hrs has no effect on cell viability (data not shown). Moreover, lysosomal damage induced by 1hr of LLOMe treatment is comparable to that of 6hrs of trehalose treatment, but a major difference between the treatments is found in the recovery phase. Indeed, trehalose induces activation of autophagy, which allows cells to recover from the lysosomal damage, preventing cell death, whereas previous studies showed that LLOMe induces a decrease in cell viability since only 50% of cells recover after LLOMe treatment (44). Thus, we could consider trehalose treatment as a disease model only at 6 hrs of treatment without considering the recovery that follows.

Here, we found that in control cells, trehalose increased lysosomal damage with a peak at 6hrs of treatment. Trehalose induced damage was reversed by WT VCP overexpression (Figure 3A,

B). On the contrary, the two VCP mutants exerted different effects: trehalose-treated cells expressing R155H VCP showed a level of lysosomal damage comparable to that observed in control cells at all time points analyzed (Figure 3B); while trehalose-treated cells expressing R191Q VCP displayed lower levels of lysosomal damage compared to control cells, but higher levels compared to cells overexpressing WT VCP. We further analyzed lysosome functionality in these conditions by evaluating lysosomal acidification (Figure 3C), using LysoTracker®, a compound highly selective for acidic organelles like lysosomes, in which its fluorescence is activated. Thus, by comparing each condition to the control, the fluorescence intensity allows evaluation of any alteration of lysosome acidification.

We found that in untreated conditions, VCP mutants decrease lysosomal acidification. A progressive decrease in acidification was also triggered by trehalose treatment, which was found to be reversed at 6 and 18hrs by the overexpression of the WT VCP, but not of the VCP mutants. Finally, we quantified lysosomal size and number at 6hrs of trehalose treatment, when lysosomal damage was most visible, and compared it to untreated conditions (Figure 3D, E). We found that trehalose treatment increased lysosomal size. This increase was prevented by the overexpression of WT VCP and only partially prevented by R191Q VCP, while R155H VCP was inactive. Moreover, we detected a trend for decreased lysosomal number in the presence of trehalose treatment, but the levels did not show any significant difference in the presence of WT VCP or mutants.

Lysosomal damage is also triggered by overexpression of some misfolded proteins, including the mutant forms of the antioxidant enzyme SOD1, which is responsible for fALS (Figure 4A, B). Therefore, we analysed the effect of WT VCP and mutants on damaged lysosomes generated upon exposure to misfolded mutant G93A SOD1 (using WT SOD1 as control). Overexpression of WT VCP fully rescued lysosomal damage induced by G93A SOD1 (Figure 4C). Conversely, the VCP mutants were unable to counteract G93A SOD1-induced lysosomal

damage, as monitored by counting the number of GFP-LGALS3 puncta (Figure 4C). We then evaluated lysosomal acidification, size, and number under these conditions (Figure 4D, E, F). G93A SOD1 decreased lysosome acidification and increased lysosomal size if compared to cells expressing WT SOD1. This was reversed by the overexpression of WT VCP, but not by the VCP mutants. As with trehalose treatment, we could not detect a significant difference in the number of lysosomes.

Together, these data indicate that enhancing WT VCP activity rescues lysosomal damage induced either by trehalose or by G93A SOD1 expression. In contrast, this protective activity of VCP is partly compromised for the disease-linked R155H and R191Q VCP mutants. The data obtained in motoneurons are in line with those collected so far in muscle (37), strongly supporting the notion that similar loss-of-function mechanisms take place in VCP associated MSP and in ALS.

VCP mutants activate autophagy.

As previously mentioned, several pieces of data, including ours, show that damaged lysosomes activate autophagy, which promotes their clearance (9,44,60). We demonstrated that VCP mutants acutely induce LMP, and unlike WT VCP, fail to rescue from lysosomal damage. Thus, we analyzed whether lysosomal damage induced by VCP mutants is capable of enhancing the autophagic flux in motoneurons. We evaluated both SQSTM1/p62 accumulation and MAP1LC3B-I conversion to MAP1LC3B-II, the lipidated and activated form, in motoneurons overexpressing WT or mutant VCP (Figure 5A-L). We performed the analyses either in basal conditions or upon NH_4Cl or chloroquine (CQ) treatment that prevents autophagolysosomal degradation of both SQSTM1/p62 and MAP1LC3B-II (61). We found increased SQSTM1/p62 levels when the autophagic flux was blocked by NH_4Cl in the presence of VCP mutants (Figure 5B). In the same conditions, we found a moderate increase in MAP1LC3B-I levels in the presence of R191Q VCP compared to control conditions (Figure

5C). By contrast, the levels of MAP1LC3B-II were increased by R155H VCP overexpression (Figure 5D). The MAP1LC3B-II/MAP1LC3B-I ratio clearly showed that both VCP mutants are able to enhance the autophagy response in motoneurons (Figure 5E). These data were confirmed and even strengthened when we used CQ to block the autophagic flux, since CQ is a stronger inhibitor of autophagy. SQSTM1/p62 and MAP1LC3B-II levels increased in the presence of both VCP mutants (Figure 5H, I). In addition, MAP1LC3B-II/MAP1LC3B-I ratio confirmed that both mutants promote autophagic flux (Figure 5I).

The levels of the monomeric soluble autophagy receptor SQSTM1/p62 were only partially increased by VCP mutants (Figure 5B), but its subcellular distribution was completely modified. In particular, R155H VCP increased the size of SQSTM1/p62 puncta (also known as SQSTM1/p62-bodies) (Figure 5M). This relocalization of SQSTM1/p62 into SQSTM1/p62-bodies is not necessarily combined with modification of the total protein levels, but it is a clear sign of activation of autophagic flux (62). Furthermore, in line with the WB data, IF analysis (Figure 5N) showed an increase in the size of MAP1LC3B puncta in the presence of VCP mutants upon NH_4Cl treatment, confirming the MAP1LC3B conversion correlated with autophagy activation. Finally, by analyzing the expression of autophagy-related genes, we found that the increase of autophagic flux was associated with autophagic gene upregulation (Figure 5O). Indeed, WT and mutant VCP promoted the expression of *SQSTM1, HSPB8, ATG-10, BECN1* genes; *ATG-12* was specifically upregulated in presence of R191Q VCP; *LAMP1* expression increased in presence of both VCP mutants. Unexpectedly, neither WT VCP nor mutants promoted *BAG3* expression. Together, these data show that VCP mutants (R155H and R191Q) selected for this study, enhance the autophagic flux.

VCP mutants specifically increase TFE3 nuclear levels.

Once determined that both VCP mutants enhance the autophagic flux and increase the expression of some autophagy-related genes, we dissected out the pathway mediating this

activity. We found that clearance of damaged lysosomes depends on transcription factors regulating the Coordinated Lysosomal Expression and Regulation (CLEAR) genes (63,64). The main CLEAR gene regulators are TFEB, a master regulator of autophagy, and TFE3.

We thus analyzed whether VCP mutants induce TFEB and TFE3 activation. Both transcription factors migrate into the nucleus only when activated. By nuclear/cytoplasmic fractionation studies, we found that while trehalose-treatment induced TFEB nuclear localization, the acute overexpression of VCP mutants did not alter TFEB localization (Figure 6A-D). Conversely, we found that nuclear TFE3 localization was enhanced by the expression of both VCP mutants; especially R191Q VCP (Figure 6A, E-G). By IF, we confirmed the nuclear TFE3 localization induced by VCP mutants (Figure 6I). As for the fractionation studies, TFEB remained confined to the cytoplasm in all VCP conditions tested (Figure 6H). Conversely, TFE3 migrated into the nucleus in presence of both VCP mutants (Figure 6I). These data differ from those of Arhzaouy *et al*. (37), who found that VCP mutants expression led to stabilization of TFEB activation, but this occurs only in very old VCP mice, while we have proved that the expression of mutant VCP is not sufficient to acutely trigger the TFEB pathway.

PPP3CB mediates TFE3 translocation induced by VCP mutants.

TFE3 nuclear translocation and activation are triggered by its dephosphorylation by the Ca^{2+}-dependent phosphatase PPP3CB (65). Thus, we silenced PPP3CB (Figure 7A) in cells overexpressing WT or mutant VCP (Figure 7B, C). We found that, while non-targeting siRNA cells showed increased GFP-TFE3 nuclear levels in the presence of VCP mutants, PPP3CB siRNA abolished TFE3 nuclear translocation induced by VCP mutants. Thus, TFE3 activation and nuclear translocation induced by VCP mutants depend on PPP3CB. This suggests that TFE3, but not TFEB, mediates the response to LMP possibly via lysosomal Ca^{2+} release in the cytoplasm, which activates PPP3CB to promote TFE3 dephosphorylation and activation.

WT VCP and mutants enhance G93A SOD1 clearance.

Since VCP mutant overexpression leads to autophagy activation, we studied if this could trigger the clearance of misfolded aggregated proteins. WT and mutants VCP were thus co-expressed with human G93A SOD1 which is unstable, misfolds and forms insoluble aggregates associated with fALS (66–68). As shown in Figure 8A, we found that the total SDS-soluble fraction of exogenous mutant human G93A SOD1 (upper band) was reduced by both WT and mutant VCP, without influencing the endogenous WT murine SOD1 (lower band). Also, the total SDS-soluble fraction of human WT SOD1 was decreased by WT VCP and R191Q VCP and totally cleared by R155H VCP (Figure 8A). Thus, WT VCP and mutants specifically clear the soluble forms of human SOD1. Using the FTA assay, we tested if WT VCP and mutants remove G93A SOD1 aggregates (Figure 8B). It is known that the PBS-insoluble G93A SOD1 levels are significantly higher than those of WT SOD1. We found that this insoluble fraction was decreased by both WT and mutant VCP in NSC-34 cells. IF analysis confirmed the decrease of G93A SOD1 aggregates in presence of VCP either WT or mutants (Figure 8D). In addition, in this condition, we observed that in the small fraction of cells containing aggregates, VCP is sequestered in the G93A SOD1 aggregates suggesting a reduction of the VCP bioavailability (and activity) in these cells (Figure 8C). Thus, WT VCP enhances the clearance of G93A SOD1 aggregates. Also, VCP mutants retain this capability in assisting misfolded protein aggregate degradation. Therefore, we suggest mutant VCP's capability to clear away misfolded protein aggregates could be correlated with autophagy activation triggered by mutant VCP induced-lysosomal damage and enhanced-autophagic flux.

Discussion

MSP or IBMPFD, FTD, and ALS are neurodegenerative/neuromuscular diseases characterized by proteostasis alterations. The most common familial forms of MSPs are associated with *VCP* mutations and the formation of ubiquitin- and TARDBP/TDP-43-positive inclusions, which are both clear signs of altered PQC (21). The PQC system is modulated by VCP and assists the removal of misfolded aggregated proteins and of altered organelles, like damaged lysosomes (9). Lysosomal damage from ruptured membranes leads to cell toxicity and death (69,70), and cells must activate their repair or degradation by lysophagy.

Here, we investigated possible pathological mechanisms for disease-associated *VCP* mutations. We found that VCP mutants accumulate into insoluble species in motoneuronal cells, and this gain of function alters cellular homeostasis. Indeed, VCP mutants also induce alterations in lysosomal size, morphology, and enzyme activity in motoneurons. These alterations partially resemble those occurring on a subset of tubular lysosomes in muscle expressing VCP mutants (71,72). We also proved that in motoneurons VCP mutants trigger lysosomal damage. Notably, WT VCP accelerates the clearance of lysosomes damaged either by specific drugs or by misfolded proteins, as demonstrated by other authors using more detrimental pharmacological approaches (9,37). Here, we demonstrated for the first time in a motoneuronal model that this protective activity of WT VCP is lost in VCP mutants, suggesting a loss of function mechanism. Thus, a dual activity co-exists for VCP mutants on lysosomal dynamics that relies on both a gain and a loss of function mechanism. The loss of VCP activity may result in defects in removing ubiquitinated proteins from damaged lysosomes, as described by Papadopoulos *et al.* (9) or in promoting autophagy induction, as shown by Hill *et al.* (36). These suggest that lysosomal damage stabilization exerted by VCP mutants could also be due to their loss of function in autophagy regulation. In any case, the presence of VCP mutants alters autophagy and lysophagy at different steps.

We found that VCP mutants positively modulate the autophagic flux, since R155H VCP increased the MAP1LC3B-I to MAP1LC3B-II conversion. MAP1LC3B-II increase is accompanied by a trend of SQSTM1/p62 accumulation into SQSTM1/p62-bodies and an upregulation of several autophagy-related genes. In addition, we demonstrated that WT VCP modulation in motoneurons leads to an increased clearance of mutant SOD1 aggregates, and this activity is retained by VCP mutants, possibly via an autophagic flux enhancement.

A novel aspect that emerged from our study is that TFE3, but not TFEB, mediates the rescue from VCP mutant-induced lysosomal damage. Lysosomal damage is known to cause activation of the CLEAR network through both TFEB and TFE3. Notably, we found that VCP mutants specifically promote TFE3, but not TFEB nuclear translocation. We also fund that in presence of VCP mutants, TFE3 activation is mediated by PPPC3B, a phosphatase triggered by increased cytoplasmic Ca^{2+}, as occurs during LMP. This finding is intriguing since, so far, only TFEB expression was studied and reported to be altered in muscles of a transgenic VCP mouse model, but at a very late stage of disease, and long after the beginning of lysosomal damage occurred (37). It would be of note to determine whether in these mice TFE3 is activated at the earliest stages, as well as if TFEB and TFE3 trigger alternative pathways.

Together, these data show an alteration of lysosome functional balance that may help to explain the presence of aberrant cytoplasmic vacuole-like structures in VCP-patients affected tissues. In line with our data, studies in *in vitro* models related to VCP mutants show the presence of abnormal autophagolysosomes (21,73) which we demonstrated to correlate with lysosomal membrane rupture followed by the activation of the autophagic flux via TFE3. Therefore, in the first stages of the disease, the activation of the autophagic pathway induced in response to VCP mutants may serve as a protective mechanism against the presence of toxic damaged lysosomes and protein aggregation. Future studies are needed to confirm these data in motor neurons *in vivo*. VCP mutants have already been proven to alter the autophagic pathway in

animal models. Therefore, it will be of interest to analyse the impact of lysosomal VCP-mutant induced damage on TFE3 regulation in these animal models or in iPSCs derived motor neurons and muscle cells. Moreover, the specific mechanisms that trigger VCP-mutant induced lysosomal damage have still to be identified. Further steps may include the analysis of the direct interaction of VCP with damaged lysosomes possibly via lysosome isolation, as well as the mechanism by which the pathway leading to PPP3CB/TEF3 activation is triggered and if this depends upon Ca^{2+} release after LMP. A deeper knowledge of these steps or of the triggering point of the damage may provide further targets for potential therapeutic approaches. Furthermore, our findings underline an important implication of VCP in counteracting SOD1 mutant pathological mechanisms such as aggregation or lysosome impairment. The testing of VCP modulation in SOD1 models could propose novel approaches also for ALS pathology. Of interest, this approach could be extended to other pathologies where lysosome alterations have been identified as Alzheimer's disease (AD) and Huntington's disease (HD) (56, 57, 59).

Collectively, our data highlight the importance of VCP in maintaining cellular homeostasis and may help to better define VCP mechanisms. This could open to a possible new pharmacological target to counteract degenerative diseases characterized by damaged lysosomes such as MSP/IBMPFD, ALS and FTD.

ACKNOWLEDGEMENTS:

We are grateful to Prof. JP Taylor (Cell & Molecular Biology Department, St. Jude Children's Research Hospital, Memphis, TN) for the FLAG-VCP WT/R155H plasmids. We are grateful to the platform NOLIMITS-Unitech (UNIMI) for the STED microscopy analysis.

FUNDING:

This research was funded by: Fondazione Telethon, Italy (n. GGP14039 to A.P., GGP19128 to A.P.); Kennedy's disease association (2018 grant to R.C.; 2020 grant to M.G.); Fondazione Cariplo, Italy (n. 2014-0686 to A.P. and S.C.; n. 2017-0747 to V.C.; 2021-1544 to R.C.); Fondazione AriSLA, Italy (n. ALS_HSPB8 to A.P.; ALS_Granulopathy to A.P. and S.C.; MLOpathy to S.C. and A.P.; Target-RAN to A.P.); Association Française contre les Myopathies, France (AFM Telethon n. 16406 and 23236 to A.P.); Università degli Studi di Milano e piano di sviluppo UNIMI—linea B (to V.C. and P.R.); Bando Straordinario per Progetti Interdipartimentali (Bando SEED 2019: #TDP-43-iPSC to V.C. and Gender-ALS to M.G.) Italian Ministry of University and Research (MIUR), PRIN—Progetti di ricerca di interesse nazionale (n. 2015LFPNMN to A.P.; n.2017F2A2C5 to A.P. and S.C.; n.2020PBS5MJ to V.C.); Fondo per il Finanziamento delle Attività Base di Ricerca (FFABR) (MIUR, to M.G., and P.R.); Agenzia Italiana del Farmaco (AIFA) (Co_ALS to A.P. and S.C.); Fondazione Regionale per la Ricerca Biomedica (FRRB) (Regione Lombardia, TRANS_ALS, project nr. 2015-0023, to A.P.): EU Joint Programme—Neurodegenerative Disease Research (JPND) project. The project is supported through the following funding organisations under the aegis of JPND—www.jpnd.eu. This project has received funding from the European Union's Horizon 2020 research and innovation programme under grant agreement N° 643417 [Grant ID: 01ED1601A, CureALS] (to A.P. and S.C.); Italian Ministry of University and Research [Progetto Dipartimenti di Eccellenza], Grant Heavy Equipment D.R. 3404, University of Genoa.

CONFLICT OF INTEREST

All authors declare no conflict of interest.

AUTHOR CONTRIBUTIONS

All authors contributed to the study conception and design. Material preparation, data collection and analysis were performed by VF, RC, PR and MEC. Statistical analysis and figure layout were performed by VF, RC and BT. Electron microscopy analysis was performed by MCG and KC. *Drosophila* maintenance and sample preparation were disposed and supervised by TRF and UBP. Mice maintenance and sample preparation were disposed and supervised by AN and MCG. The first draft of the manuscript was written by AP and KC and all authors commented on previous versions of the manuscript. All authors read and approved the final manuscript.

ETHICAL APPROVAL

All experiments on mice were executed with the approval of the Institutional Animal Care and Use Committee (IACUC) at University of California, Irvine (UCI) (IACUC Protocol #AUP-19-075), and in accordance with the guidelines established by the National Institutes of Health (NIH).

References

1. Koller KJ, Brownstein MJ. Use of a cDNA clone to identify a supposed precursor protein containing valosin. Nature. 1987 Feb;325(6104):542–5.
2. Moir D, Stewart SE, Osmond BC, Botstein D. Cold-sensitive cell-division-cycle mutants of yeast: isolation, properties, and pseudoreversion studies. Genetics. 1982 Apr;100(4):547–63.
3. Wang Q, Song C, Li CCH. Molecular perspectives on p97-VCP: Progress in understanding its structure and diverse biological functions. J Struct Biol. 2004 Apr;146(1-2):44-57.
4. Buchberger A, Schindelin H, Hänzelmann P. Control of p97 function by cofactor binding. FEBS Lett. 2015 Sep;589(19PartA):2578–89.
5. Latterich M, Fröhlich KU, Schekman R. Membrane fusion and the cell cycle: Cdc48p participates in the fusion of ER membranes. Cell. 1995 Sep;82(6):885–93.
6. Acharya U, Jacobs R, Peters JM, Watson N, Farquhar MG, Malhotra V. The formation of golgi stacks from vesiculated golgi membranes requires two distinct fusion events. Cell. 1995 Sep;82(6):895–904.
7. Ramanathan HN, Ye Y. The p97 ATPase associates with EEA1 to regulate the size of early endosomes. Cell Res. 2012 Feb;22(2):346–59.
8. Xu S, Peng G, Wang Y, Fang S, Karbowsk M. The AAA-ATPase p97 is essential for outer mitochondrial membrane protein turnover. Mol Biol Cell. 2011 Feb;22(3):291–300.
9. Papadopoulos C, Kirchner P, Bug M, Grum D, Koerver L, Schulze N, et al. VCP/p97 cooperates with YOD1, UBXD1 and PLAA to drive clearance of ruptured lysosomes by autophagy. EMBO J. 2017 Jan;36(2):135–50.
10. Madeo F, Schlauer J, Zischka H, Mecke D, Fröhlich K-U. Tyrosine Phosphorylation Regulates Cell Cycle-dependent Nuclear Localization of Cdc48p. Mol Biol Cell. 1998 Jan;9(1):131–41.
11. Meerang M, Ritz D, Paliwal S, Garajova Z, Bosshard M, Mailand N, et al. The ubiquitin-selective segregase VCP/p97 orchestrates the response to DNA double-strand breaks. Nat Cell Biol. 2011 Nov;13(11):1376–82.
12. Verma R, Oania RS, Kolawa NJ, Deshaies RJ. Cdc48/p97 promotes degradation of aberrant nascent polypeptides bound to the ribosome. Elife. 2013 Jan; 2:e00308.
13. van den Boom J, Meyer H. VCP/p97-Mediated Unfolding as a Principle in Protein Homeostasis and Signaling. Mol Cell. 2018 Jan;69(2):182-194..
14. Meyer H, Bug M, Bremer S. Emerging functions of the VCP/p97 AAA-ATPase in the ubiquitin system. Nat Cell Biol. 2012 Feb;14(2):117–23.
15. Stein A, Ruggiano A, Carvalho P, Rapoport TA. Key Steps in ERAD of Luminal ER Proteins Reconstituted with Purified Components. Cell. 2014 Sep;158(6):1375–88.
16. Franz A, Ackermann L, Hoppe T. Ring of Change: CDC48/p97 Drives Protein Dynamics at Chromatin. Front Genet. 2016 May;7:73.
17. Tanaka A, Cleland MM, Xu S, Narendra DP, Suen D-FF, Karbowski M, et al. Proteasome and p97 mediate mitophagy and degradation of mitofusins induced by Parkin. J Cell Biol. 2010 Dec;191(7):1367–80.
18. Krick R, Bremer S, Welter E, Schlotterhose P, Muehe Y, Eskelinen E-L, et al. Cdc48/p97 and Shp1/p47 regulate autophagosome biogenesis in concert with ubiquitin-like Atg8. J Cell Biol. 2010 Sep;190(6):965–73.
19. Anderson DJ, Le Moigne R, Djakovic S, Kumar B, Rice J, Wong S, et al. Targeting the AAA ATPase p97 as an Approach to Treat Cancer through Disruption of Protein Homeostasis. Cancer Cell. 2015 Nov;28(5):653–65.

20. Watts GDJ, Wymer J, Kovach MJ, Mehta SG, Mumm S, Darvish D, et al. Inclusion body myopathy associated with Paget disease of bone and frontotemporal dementia is caused by mutant valosin-containing protein. Nat Genet. 2004 Apr;36(4):377–81.
21. Johnson JO, Mandrioli J, Benatar M, Abramzon Y, Van Deerlin VM, Trojanowski JQ, et al. Exome sequencing reveals VCP mutations as a cause of familial ALS. Neuron. 2010 Dec;68(5):857–64.
22. Chan N, Le C, Shieh P, Mozaffar T, Khare M, Bronstein J, et al. Valosin-containing protein mutation and Parkinson's disease. Parkinsonism Relat Disord. 2012 Jan;18(1):107-9.
23. Taylor JP. Multisystem proteinopathy: intersecting genetics in muscle, bone, and brain degeneration. Neurology. 2015 Aug;85(8):658–60.
24. Le Ber I, Van Bortel I, Nicolas G, Bouya-Ahmed K, Camuzat A, Wallon D, et al. hnRNPA2B1 and hnRNPA1 mutations are rare in patients with "multisystem proteinopathy" and frontotemporal lobar degeneration phenotypes. Neurobiol Aging. 2014 Apr;35(4):934.e5-6.
25. Tang WK, Li D, Li C, Esser L, Dai R, Guo L, et al. A novel ATP-dependent conformation in p97 N-D1 fragment revealed by crystal structures of disease-related mutants. EMBO J. 2010 Jul;29(13):2217–29.
26. Tang WK, Xia D. Altered intersubunit communication is the molecular basis for functional defects of pathogenic p97 mutants. J Biol Chem. 2013 Dec;288(51):36624–35.
27. Hänzelmann P, Buchberger A, Schindelin H. Hierarchical binding of cofactors to the AAA ATPase p97. Structure. 2011 Jun;19(6):833–43.
28. Fernández-Sáiz V, Buchberger A. Imbalances in p97 co-factor interactions in human proteinopathy. EMBO Rep. 2010 Jun;11(6):479–85.
29. Tang WK, Xia D. Mutations in the Human AAA+ Chaperone p97 and Related Diseases. Front Mol Biosci. 2016 Dec;3:79.
30. Hemion C, Flammer J, Neutzner A. Quality control of oxidatively damaged mitochondrial proteins is mediated by p97 and the proteasome. Free Radic Biol Med. 2014 Oct;75:121–8.
31. Meyer HH. Golgi reassembly after mitosis: The AAA family meets the ubiquitin family. Biochim Biophys Acta - Mol Cell Res. 2005 Jun;1744(2):108–19.
32. Neal S, Mak R, Bennett EJ, Hampton R. A Cdc48 "Retrochaperone" Function Is Required for the Solubility of Retrotranslocated, Integral Membrane Endoplasmic Reticulum-associated Degradation (ERAD-M) Substrates. J Biol Chem. 2017 Feb;292(8):3112–28.
33. Schweitzer K, Pralow A, Naumann M. p97/VCP promotes Cullin-RING-ubiquitin-ligase/proteasome-dependent degradation of IκBα and the preceding liberation of RelA from ubiquitinated IκBα. J Cell Mol Med. 2016 Jan;20(1):58–70.
34. Wrobel L, Hill SM, Ashkenazi A, Rubinsztein DC. VCP/p97 modulates PtdIns3P production and autophagy initiation. Autophagy. 2021 Apr;17(4):1052–3.
35. Ju J-S, Fuentealba RA, Miller SE, Jackson E, Piwnica-Worms D, Baloh RH, et al. Valosin-containing protein (VCP) is required for autophagy and is disrupted in VCP disease. J Cell Biol. 2009 Dec;187(6):875–88.
36. Hill SM, Wrobel L, Ashkenazi A, Fernandez-Estevez M, Tan K, Bürli RW, et al. VCP/p97 regulates Beclin-1-dependent autophagy initiation. Nat Chem Biol. 2021 Apr;17(4):448–55.
37. Arhzaouy K, Papadopoulos C, Schulze N, Pittman SK, Meyer H, Weihl CC. VCP maintains lysosomal homeostasis and TFEB activity in differentiated skeletal muscle. Autophagy. 2019 Jun;15(6):1082–99.

38. Roczniak-Ferguson A, Petit CS, Froehlich F, Qian S, Ky J, Angarola B, et al. The transcription factor TFEB links mTORC1 signaling to transcriptional control of lysosome homeostasis. Sci Signal. 2012 Jun;5(228):ra42.
39. Simeoni S, Mancini MA, Stenoien DL, Marcelli M, Weigel NL, Zanisi M, et al. Motoneuronal cell death is not correlated with aggregate formation of androgen receptors containing an elongated polyglutamine tract. Hum Mol Genet. 2000 Jan;9(1):133–44.
40. Badadani M, Nalbandian A, Watts GD, Vesa J, Kitazawa M, Su H, et al. VCP Associated Inclusion Body Myopathy and Paget Disease of Bone Knock-In Mouse Model Exhibits Tissue Pathology Typical of Human Disease. PLoS One. 2010 Oct;5(10):e13183.
41. Ritson GP, Custer SK, Freibaum BD, Guinto JB, Geffel D, Moore J, et al. TDP-43 mediates degeneration in a novel Drosophila model of disease caused by mutations in VCP/p97. J Neurosci. 2010 Jun;30(22):7729–39.
42. Kour S, Rajan DS, Fortuna TR, Anderson EN, Ward C, Lee Y, et al. Loss of function mutations in GEMIN5 cause a neurodevelopmental disorder. Nat Commun. 2021 Dec;12(1):2558.
43. Ramesh N, Kour S, Anderson EN, Rajasundaram D, Pandey UB. RNA-recognition motif in Matrin-3 mediates neurodegeneration through interaction with hnRNPM. Acta Neuropathol Commun. 2020 Dec;8(1):138.
44. Rusmini P, Cortese K, Crippa V, Cristofani R, Cicardi ME, Ferrari V, et al. Trehalose induces autophagy via lysosomal-mediated TFEB activation in models of motoneuron degeneration. Autophagy. 2019 Apr;15(4):631–51.
45. Settembre C, Medina DL. TFEB and the CLEAR network. Methods Cell Biol. 2015 Jan;126:45–62.
46. Klickstein JA, Mukkavalli S, Raman M. AggreCount: an unbiased image analysis tool for identifying and quantifying cellular aggregates in a spatially defined manner. J Biol Chem. 2020 Dec;295(51):17672–83.
47. Nalbandian A, Llewellyn KJ, Kitazawa M, Yin HZ, Badadani M, Khanlou N, et al. The Homozygote VCPR155H/R155H Mouse Model Exhibits Accelerated Human VCP-Associated Disease Pathology. PLoS One. 2012 Sep;7(9):e46308.
48. Watts G, Thomasova D, Ramdeen S, Fulchiero E, Mehta S, Drachman D, et al. Novel VCP mutations in inclusion body myopathy associated with Paget disease of bone and frontotemporal dementia. Clin Genet. 2007 Oct;72(5):420–6.
49. Alroy J, Garganta C, Wiederschain G. Secondary biochemical and morphological consequences in lysosomal storage diseases. Biochemistry (Mosc). 2014 Jul;79(7):619–36.
50. Ferreira CR, Gahl WA. Lysosomal storage diseases. Transl Sci rare Dis. 2017 May;2(1–2):1–71.
51. García-Sanz P, Orgaz L, Fuentes JM, Vicario C, Moratalla R. Cholesterol and multilamellar bodies: Lysosomal dysfunction in GBA-Parkinson disease. Autophagy. 2018 Apr;14(4):717–8.
52. Maier O, Böhm J, Dahm M, Brück S, Beyer C, Johann S. Differentiated NSC-34 motoneuron-like cells as experimental model for cholinergic neurodegeneration. Neurochem Int. 2013 Jun;62(8):1029–38.
53. Crippa V, Sau D, Rusmini P, Boncoraglio A, Onesto E, Bolzoni E, et al. The small heat shock protein B8 (HspB8) promotes autophagic removal of misfolded proteins involved in amyotrophic lateral sclerosis (ALS). Hum Mol Genet. 2010 Sep;19(17):3440–56.
54. Crippa V, Cicardi ME, Ramesh N, Seguin SJ, Ganassi M, Bigi I, et al. The chaperone HSPB8 reduces the accumulation of truncated TDP-43 species in cells and protects against TDP-43-mediated toxicity. Hum Mol Genet. 2016 Sep;25(18):3908–24.

55. Bayraktar O, Oral O, Kocaturk NM, Akkoc Y, Eberhart K, Kosar A, et al. IBMPFD Disease-Causing Mutant VCP/p97 Proteins Are Targets of Autophagic-Lysosomal Degradation. Srinivasula SM, editor. PLoS One. 2016 Oct;11(10):e0164864.
56. Hirakura Y, Kagan BL. Pore formation by beta-2-microglobulin: A mechanism for the pathogenesis of dialysis associated amyloidosis. Amyloid. 2001 Jun;8(2):94–100.
57. Lin H, Bhatia R, Lal R. Amyloid β protein forms ion channels: implications for Alzheimer's disease pathophysiology. FASEB J. 2001 Nov;15(13):2433–44.
58. Radford SE, Dobson CM. From computer simulations to human disease: Emerging themes in protein folding. Cell. 1999 Apr;97(3):291-8.
59. Ross CA. Polyglutamine pathogenesis: Emergence of unifying mechanisms for Huntington's disease and related disorders. Neuron. 2002 Aug 29;35(5):819-22.
60. Maejima I, Takahashi A, Omori H, Kimura T, Takabatake Y, Saitoh T, et al. Autophagy sequesters damaged lysosomes to control lysosomal biogenesis and kidney injury. EMBO J. 2013 Aug;32(17):2336–47.
61. Amenta JS, Hlivko TJ, McBee AG, Shinozuka H, Brocher S. Specific inhibition by NH4Cl of autophagy-associated proteolysis in cultured fibroblasts. Exp Cell Res. 1978 Sep;115(2):357–66.
62. BenYounès A, Tajeddine N, Tailler M, Malik SA, Shen S, Métivier D, et al. A fluorescence-microscopic and cytofluorometric system for monitoring the turnover of the autophagic substrate p62/SQSTM1. Autophagy. 2011 Aug;7(8):883–91.
63. Sardiello M, Palmieri M, di Ronza A, Medina DL, Valenza M, Gennarino VA, et al. A Gene Network Regulating Lysosomal Biogenesis and Function. Science. 2009 Jul;325(5939):473-7.
64. Settembre C, Di Malta C, Polito VA, Garcia Arencibia M, Vetrini F, Erdin S, et al. TFEB links autophagy to lysosomal biogenesis. Science. 2011 Jun;332(6036):1429–33.
65. Medina DL, Di Paola S, Peluso I, Armani A, De Stefani D, Venditti R, et al. Lysosomal calcium signalling regulates autophagy through calcineurin and TFEB. Nat Cell Biol. 2015 Mar;17(3):288–99.
66. Bendotti C, Marino M, Cheroni C, Fontana E, Crippa V, Poletti A, et al. Dysfunction of constitutive and inducible ubiquitin-proteasome system in amyotrophic lateral sclerosis: Implication for protein aggregation and immune response. Prog Neurobiol. 2012 May;97(2):101-26.
67. Crippa V, Carra S, Rusmini P, Sau D, Bolzoni E, Bendotti C, et al. A role of small heat shock protein B8 (HspB8) in the autophagic removal of misfolded proteins responsible for neurodegenerative diseases. Autophagy. 2010 Oct;6(7):958–60.
68. Sau D, De Biasi S, Vitellaro-Zuccarello L, Riso P, Guarnieri S, Porrini M, et al. Mutation of SOD1 in ALS: a gain of a loss of function. Hum Mol Genet. 2007 Jul;16(13):1604–1618.
69. Aits S, Jäättelä M. Lysosomal cell death at a glance. J Cell Sci. 2013 May;126(9):1905–12.
70. Wang C, Telpoukhovskaia MA, Bahr BA, Chen X, Gan L. Endo-lysosomal dysfunction: a converging mechanism in neurodegenerative diseases. Curr Opin Neurobiol. 2018 Feb;48:52–8.
71. Johnson AE, Shu H, Hauswirth AG, Tong A, Davis GW. VCP-dependent muscle degeneration is linked to defects in a dynamic tubular lysosomal network in vivo. Elife. 2015 Jul;4:e07366.
72. Johnson AE, Orr BO, Fetter RD, Moughamian AJ, Primeaux LA, Geier EG, et al. SVIP is a molecular determinant of lysosomal dynamic stability, neurodegeneration and lifespan. Nat Commun. 2021 Jan;12(1):1–17.
73. Tresse E, Salomons FA, Vesa J, Bott LC, Kimonis V, Yao T-P, et al. VCP/p97 is

essential for maturation of ubiquitin-containing autophagosomes and this function is impaired by mutations that cause IBMPFD. Autophagy. 2010 Feb;6(2):217–27.

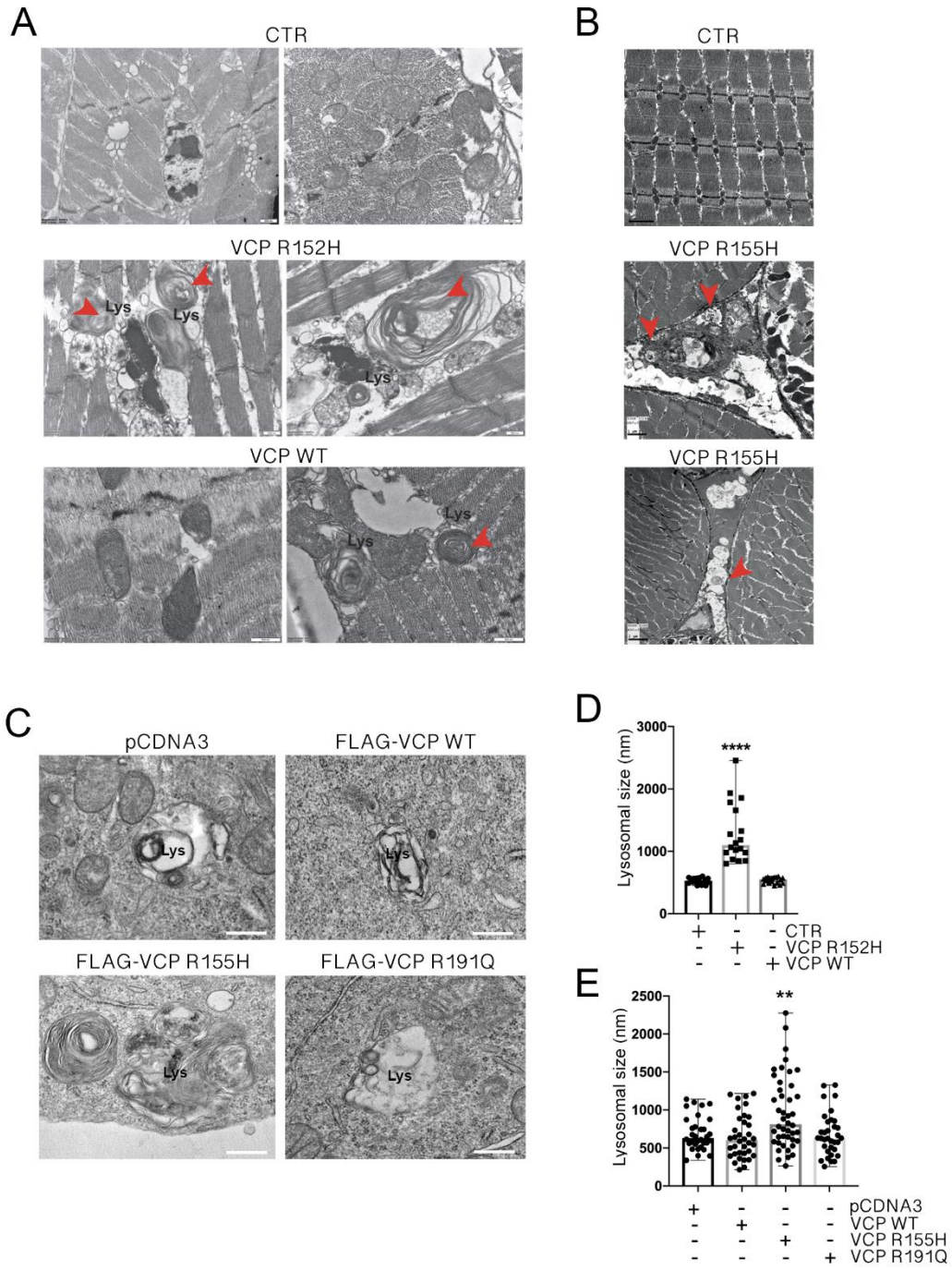

Figure 1. Abnormal lysosomal structures in tissues and cells expressing mutant VCPs. (A) Electron microscopy analysis of lysosomes in thoracic muscle of *Drosophila melanogaster* expressing either WT (CTR) or R152H mutation. Scale bar, 600 nm. Red arrows evidence MLBs. (B) Electron microscopy analysis of lysosomes in quadriceps muscles of control (CTR) and transgenic R155H VCP mice. Scale bar, 1 µm or 2 µm. Red arrows evidence MLBs. (C) Electron microscopy analysis of lysosomes in NSC-34 expressing WT or mutants FLAG-

VCPs. Scale bar, 200 nm. (D) The bar graph represents lysosomal diameters measured on EM analysis of *Drosophila melanogaster* expressing either WT (CTR) or R152H mutation. 32-42 lysosomes were analyzed for each condition (Kruskal-Wallis test followed by Dunn's multiple comparison test; ****$p<0.0001$). (E) The bar graph represents lysosomal diameters measured on EM analysis of NSC-34 expressing WT or mutants FLAG-VCPs. 33-42 lysosomes were analyzed for each condition (Kruskal-Wallis test followed by Dunn's multiple comparison test; **$p<0.01$).

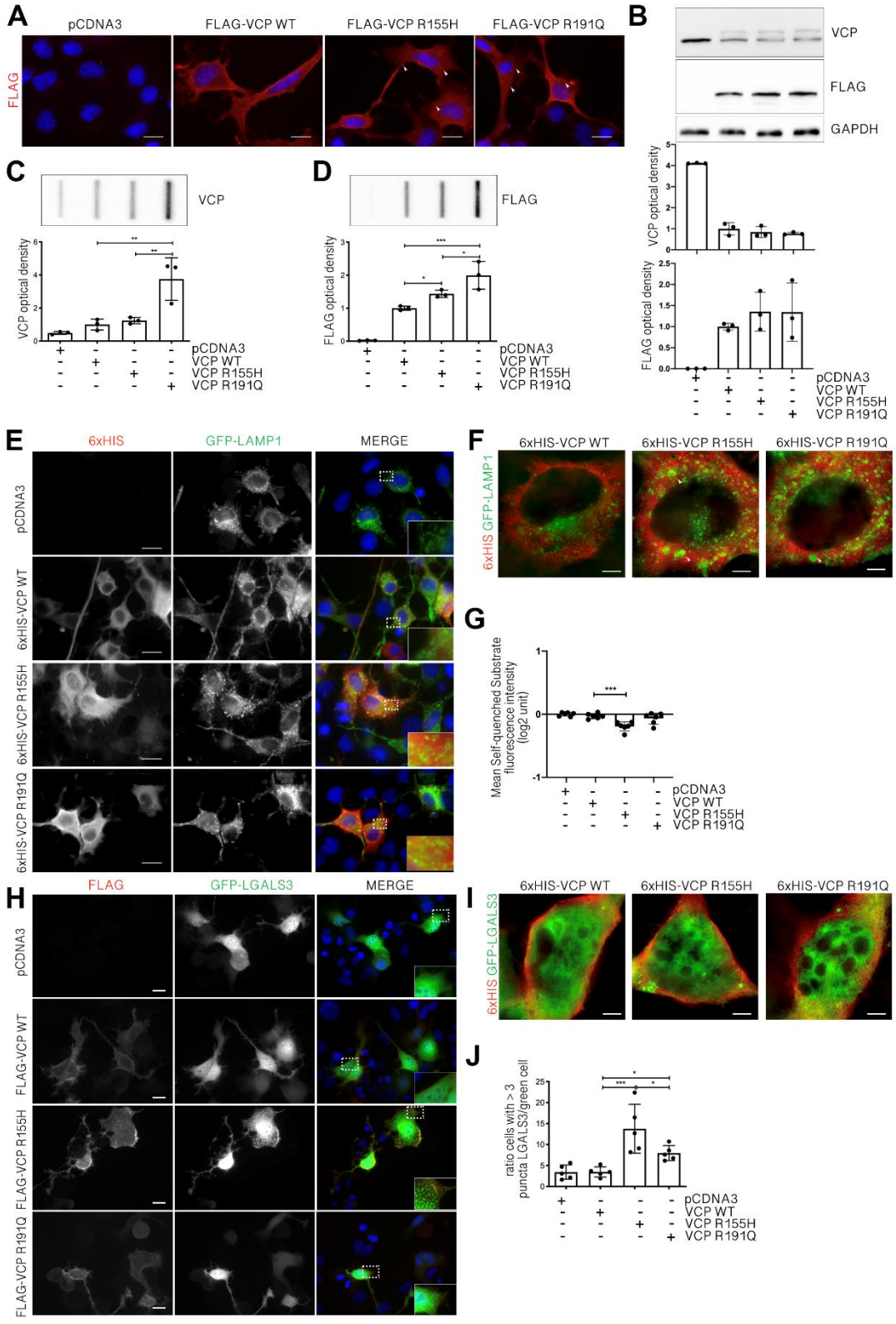

Figure 2. VCP mutants aggregate and induce lysosomal damage in NSC-34. (A) IF microscopy analysis (63x magnification) on NSC-34 cells overexpressing WT or mutants FLAG-VCPs. Nuclei were stained with DAPI (blue), while FLAG-VCP with the anti-FLAG antibody (red). Scale bar, 10 μm. (B) A representative WB analysis of PBS extracts of NSC-34 overexpressing

WT or mutants FLAG-VCPs. To visualize total VCP, an anti-VCP antibody was used. To visualize exogenous FLAG-VCP, an anti-FLAG antibody was used. GAPDH was used as loading control (upper inset). Optical densitometry quantification of VCP in WB was computed over three independent biological samples for each condition (n=3) ± SD (middle inset). Optical densitometry quantification of FLAG-VCP in WB (lower inset) computed over three independent biological samples for each condition (n=3) ± SD (one-way ANOVA followed by Fisher's LSD test). (C, D) FTA (upper inset) of PBS extracts of NSC-34 overexpressing WT or mutants FLAG-VCPs. To visualize total VCP, an anti-VCP antibody was used (C). To visualize exogenous FLAG-VCP, an anti-FLAG antibody was used (D). Bar graph represents FTA mean relative optical density computed over three independent biological samples for each condition (n=3) ± SD (one-way ANOVA followed by Fisher's LSD test; *$p<0.05$, **$p<0.01$, ***$p<0.001$). (E) IF microscopy analysis (63x magnification) on NSC-34 cells overexpressing WT or mutants 6xHIS-VCPs and GFP-LAMP1. 6xHIS-VCPs were stained with an anti-6xHIS antibody (red), LAMP1 was visualized as GFP-LAMP1 (green), and nuclei were stained with DAPI (blue). A 2.5x magnification of selected areas is shown. Scale bar, 10 μm. (F) STED microscopy analysis on NSC-34 cells overexpressing WT or mutants 6xHIS-VCPs and GFP-LAMP1. 6xHIS-VCPs were stained with an anti-6xHIS antibody (red) and LAMP1 was visualized as GFP-LAMP1 (green). Scale bar, 5 μm. (G) Cytofluorimetric analysis performed on NSC-34 cells overexpressing WT or mutants FLAG-VCPs treated with Lysosome-Specific Self-Quenched Substrate. Mean fluorescence intensity was measured (n=6) (one-way ANOVA followed by Fisher's LSD test; ***$p<0.001$). (H) IF microscopy analysis (40x magnification) on NSC-34 cells overexpressing WT or mutants FLAG-VCPs and GFP-LGALS3. FLAG-VCPs were stained with an anti-FLAG antibody (red), galectin-3 was visualized as GFP-LGALS3 (green), and nuclei were stained with DAPI (blue). A 2x magnification of selected areas is shown. Scale bar, 10 μm. (I) STED microscopy analysis on NSC-34 cells overexpressing WT or mutants 6xHIS -VCPs and GFP-LGALS3. 6xHIS tagged VCPs were detected using an anti-6xHIS antibody red and galectin-3 as GFP-LGALS3 (green). Scale bar, 5 μm (J) The bar graph represents the quantification of the percentage of cells with >3 GFP-LGALS3 puncta after transfection with pCDNA3, WT or mutants FLAG-VCPs; the fields were randomly selected and at least 100 cells for each sample were counted over 5 independent biological samples for each condition (n=5) ± SD (One-way ANOVA followed by Fisher's LSD test; *$p<0.05$, ***$p<0.001$).

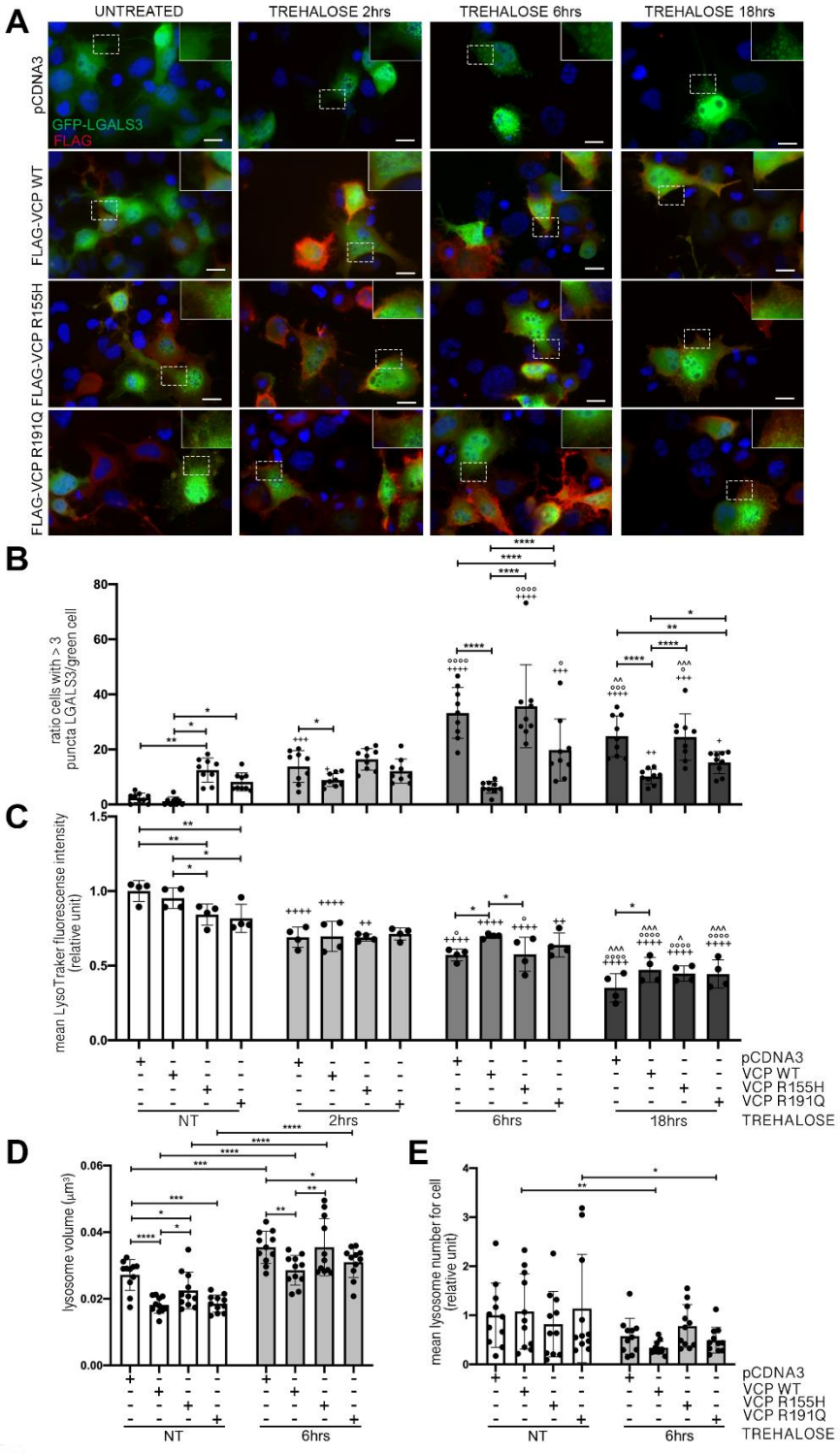

Figure 3. WT VCP modulation decrease levels of chemically damaged lysosomes. (A) IF microscopy analysis (40x magnification) on NSC-34 cells overexpressing WT or mutants FLAG-VCPs and GFP-LGALS3 and treated with trehalose for different time points. FLAG-VCPs were stained with anti-FLAG antibody (red), galectin-3 was visualized as GFP-LGALS3 (green), and nuclei were stained with DAPI (blue). A 2x magnification of selected areas is shown. Scale bar, 10 µm. (B) The bar graph represents the quantification of percentage of cells

with >3 GFP-LGALS3 puncta after transfection with pCDNA3, WT or mutants FLAG-VCPs, and after trehalose treatment at different time points; the fields were randomly selected and at least 100 cells for each sample were counted over 9 independent biological samples for each condition (n=9) ± SD (Two-way ANOVA with Fisher's LSD test; *p<0.05, **p<0.01, ****p<0.0001; $^{+}$p<0.05, $^{++}$p<0.01, $^{+++}$p<0.001, $^{++++}$p<0.0001, vs NT; °p<0.05, °°°p<0.001, °°°°p<0.0001, vs 2 hrs trehalose; ^^p<0.01, ^^^p<0.001, vs 6 hrs trehalose). (C) The bar graph represents the quantification of the mean LysoTracker fluorescence intensity cytofluorimetric analysis performed on NSC-34 cells overexpressing WT or mutants FLAG-VCPs, treated with trehalose for different time periods and labelled with LysoTracker Green. Mean fluorescence intensity was measured (n = 4) (Two-way ANOVA with Fisher's LSD test; *p<0.05, **p<0.01; $^{++}$p<0.01, $^{++++}$p<0.0001, vs NT; °p<0.05, °°°°p<0.0001, vs 2hrs trehalose; ^p<0.05, ^^^p<0.001, vs 6hrs trehalose). (D) The bar graph represents the quantification of lysosome volume of NSC-34 after transfection with pCDNA3, WT or mutants FLAG-VCPs, and after 6hrs trehalose treatment. The fields were randomly selected and at least 50 cells for each sample were counted over 11 independent biological samples for each condition (n=11) ± SD (Two-way ANOVA with Fisher's LSD test; *p<0.05, **p<0.01, ***p<0.001, ****p<0.0001) (E) The bar graph represents the number of lysosomes of NSC-34 after transfection with pCDNA3, WT or mutants FLAG-VCPs, and after 6hrs trehalose treatment. The fields were randomly selected and at least 50 cells for each sample were counted over 11 independent biological samples for each condition (n=11) ± SD (Two-way ANOVA with Fisher's LSD test; *p<0.05, **p<0.01).

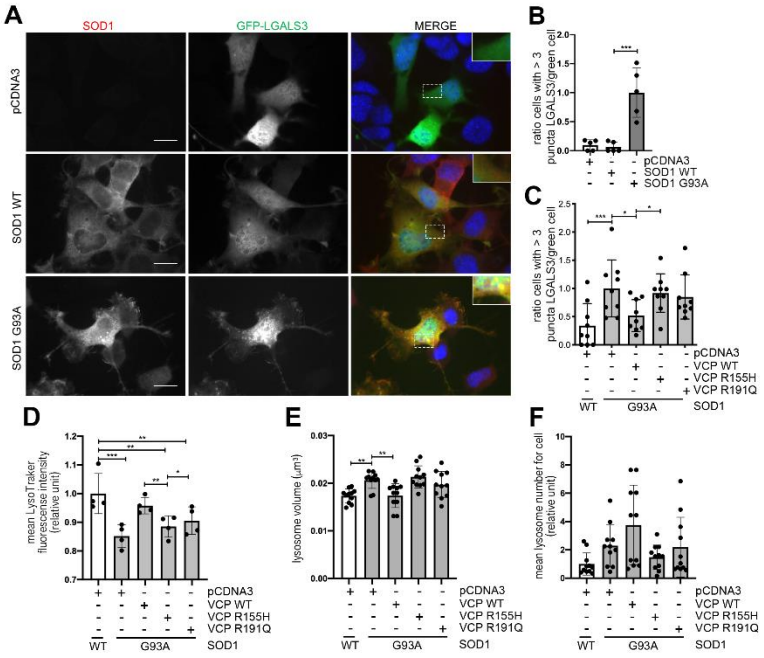

Figure 4. WT VCP modulation decrease levels of lysosomal damage induced by SOD1 mutant. (A) IF microscopy analysis (63x magnification) on NSC-34 cells overexpressing WT SOD1 or G93A SOD1 and GFP-LGALS3. SOD1 was stained with an anti-SOD1 antibody (red), galectin-3 was visualized as GFP-LGALS3 (green), and nuclei were stained with DAPI (blue). A 2x magnification of selected areas is shown. Scale bar, 10 µm. (B) The bar graph represents the quantification of percentage of cells with >3 GFP-LGALS3 puncta after transfection with pCDNA3, WT SOD1 or G93A SOD1; the fields were randomly selected and at least 100 cells for each sample were counted over 5 independent biological samples for each condition (n=5) ± SD (Unpaired t-test with Welch's correction; **p<0.001) (C) The bar graph represents the quantification of percentage of cells with >3 GFP-LGALS3 puncta after transfection with pCDNA3, WT or mutants FLAG-VCPs and WT SOD1 or G93A SOD1; the fields were randomly selected and at least 100 cells for each sample were counted over 9 independent biological samples for each condition (n=9) ± SD (One-way ANOVA followed by Fisher's LSD test; *p<0.05, ***p<0.001). (D) The bar graph represents the quantification of the mean LysoTracker fluorescence intensity cytofluorimetric analysis performed on NSC-34 transfected with pCDNA3, WT or mutants FLAG-VCPs and WT SOD1 or G93A SOD1 periods and labelled with LysoTracker Green. Mean fluorescence intensity was measured (n =

4) (One-way ANOVA with Fisher's LSD test; *p<0.05, **p<0.01, ***p<0.001). (E) The bar graph represents the quantification of lysosome volume of NSC-34 transfected with pCDNA3, WT or mutants FLAG-VCPs and WT SOD1 or G93A SOD1. The fields were randomly selected and at least 50 cells for each sample were counted over 11 independent biological samples for each condition (n=11) ± SD (One-way ANOVA with Fisher's LSD test; **p<0.01) (F) The bar graph represents the number of lysosomes of NSC-34 after transfection pCDNA3, WT or mutants FLAG-VCPs and WT SOD1 or G93A SOD1. The fields were randomly selected and at least 50 cells for each sample were counted over 11 independent biological samples for each condition (n=11) ± SD (One-way ANOVA with Fisher's LSD test).

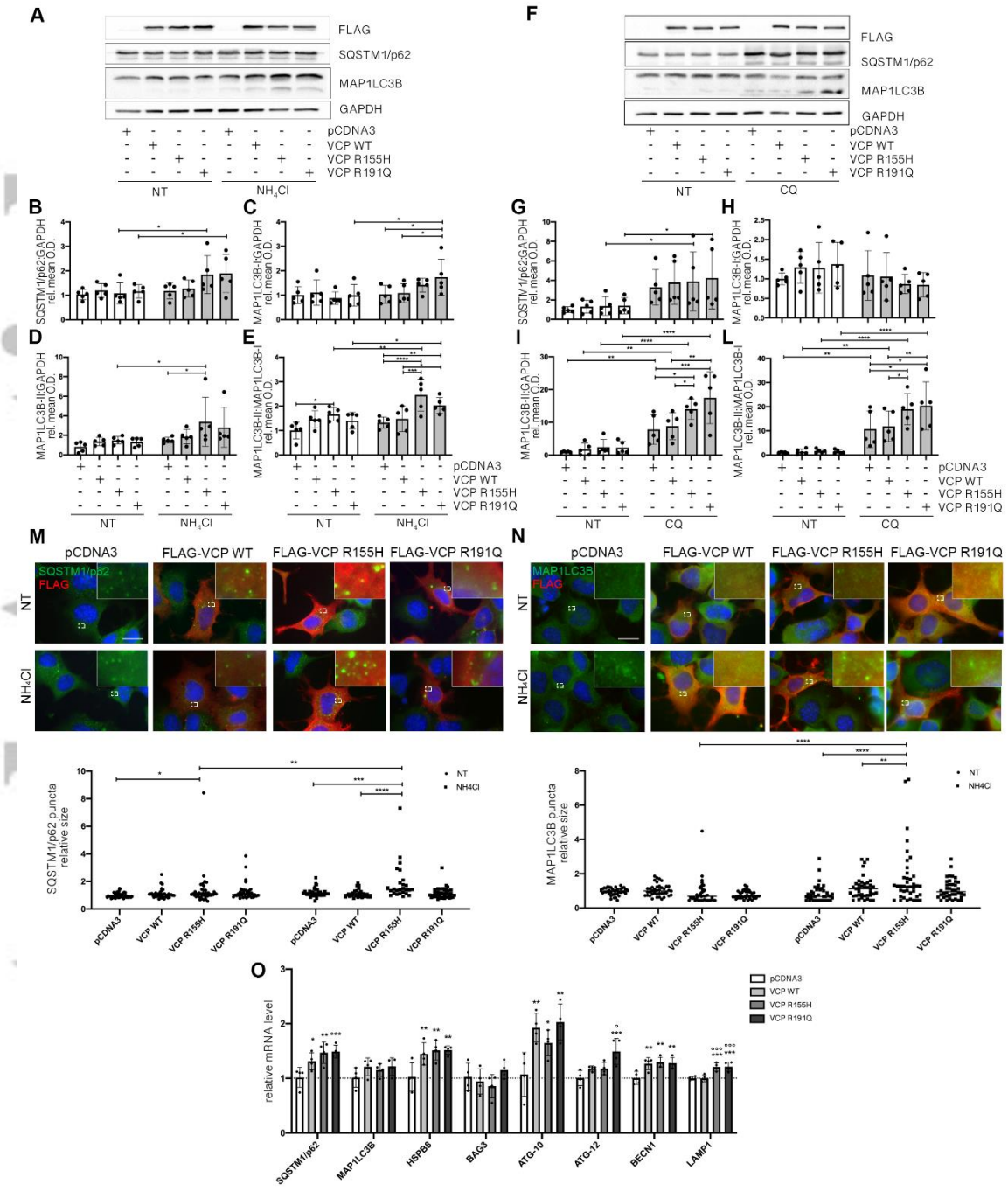

Figure 5. VCP mutants activate autophagy. (A) A representative WB of PBS extracts of NSC-34 overexpressing WT or mutants FLAG-VCPs and treated with NH_4Cl. To visualize FLAG-VCP, an anti-FLAG antibody was used. To visualize the autophagic markers MAP1LC3B and SQSTM1/p62, an anti-MAP1LC3B antibody and an anti-SQSTM1/p62 antibody were used respectively. GAPDH was used as loading control. (B-E) Quantification of WB analysis presented in Figure A. (B) The bar graph represents the mean relative optical density quantification of SQSTM1/p62 detected by WB using an anti-SQSTM1/p62 antibody. (C) The bar graph represents the mean relative optical density quantification of MAP1LC3B-I detected

by WB (upper lane considered) using an anti-MAP1LC3B antibody. (D) The bar graph represents the mean relative optical density quantification of MAP1LC3B-II detected by WB (lower lane considered) using an anti-MAP1LC3B antibody. (E) The bar graph represents the ratio of the mean relative optical density quantification of MAP1LC3B-II detected by WB (lower lane considered) and of the mean relative optical density quantification of MAP1LC3B-I detected by WB (upper lane) using an anti-MAP1LC3B antibody. All quantification histograms were calculated using the mean ±SD for n=5 independent replicates. (Two-way ANOVA with Fisher's LSD test; *p< 0.05, **p < 0.01, ***p<0.001, ****p<0.0001). (F) A representative WB of PBS extracts of NSC-34 overexpressing WT or mutants FLAG-VCPs and treated with CQ. (G-L) Quantification of WB analysis presented in Figure F. (G) The bar graph represents the mean relative optical density quantification of SQSTM1/p62 detected by WB using an anti-SQSTM1/p62 antibody. (H) The bar graph represents the mean relative optical density quantification of MAP1LC3B-I detected by WB (upper lane considered) using an anti-MAP1LC3B antibody. (I) The bar graph represents the mean relative optical density quantification of MAP1LC3B-II detected by WB (lower lane considered) using an anti-MAP1LC3B antibody. (L) The bar graph represents the ratio of the mean relative optical density quantification of MAP1LC3B-II detected by WB (lower lane considered) and of the mean relative optical density quantification of MAP1LC3B-I detected by WB (upper lane) using an anti-MAP1LC3B antibody. All quantification histograms were calculated using the mean ±SD for n=5 independent replicates. (Two-way ANOVA with Fisher's LSD test; *p< 0.05, **p < 0.01, ***p<0.001, ****p<0.0001). (M) IF microscopy analysis (63x magnification) of NSC-34 overexpressing WT or mutants FLAG-VCPs (upper inset). FLAG-VCP was stained with an anti-FLAG antibody (red), SQSTM1/p62 was stained with an anti-SQSTM1/p62 antibody (green), and nuclei were stained with DAPI (blue). An 8x magnification of selected areas is shown. Scale bar, 10 μm. The bar graph (lower inset) represents quantification of SQSTM1/p62 puncta average size per cell. 40 cells were analysed for each condition (two-way ANOVA with Dunnett's test and Šidák's test *p < 0.05, ** p < 0.01, ***p<0.001, ****p<0.0001). (N) IF microscopy analysis (63x magnification) of NSC-34 overexpressing WT or mutants FLAG-VCPs (upper inset). FLAG-VCP was stained with an anti-FLAG antibody (red), MAP1LC3B was stained with an anti-MAP1LC3B antibody (green), and nuclei were stained with DAPI (blue). An 8x magnification of selected areas is shown. Scale bar, 10 μm. The bar graph (lower inset) represents quantification of MAP1LC3B puncta average size per cell. 40 cells were analysed for each condition (two-way ANOVA with

Dunnett's test and Šidák's test; **p < 0.01, ****p<0.0001). (O) RT-qPCR for SQSTM1/p62, MAP1LC3B, HSPB8, BAG3, ATG-10, ATG-12, BECN1, LAMP1 mRNA normalized with Rplp0 mRNA levels. Data are means ± SD of 4 independent samples (One-way ANOVA with Fisher's LSD test; *p< 0.05, **p < 0.01, ***p<0.001 vs pCDNA3; °p<0.05, °°°p<0.001 vs WT VCP)

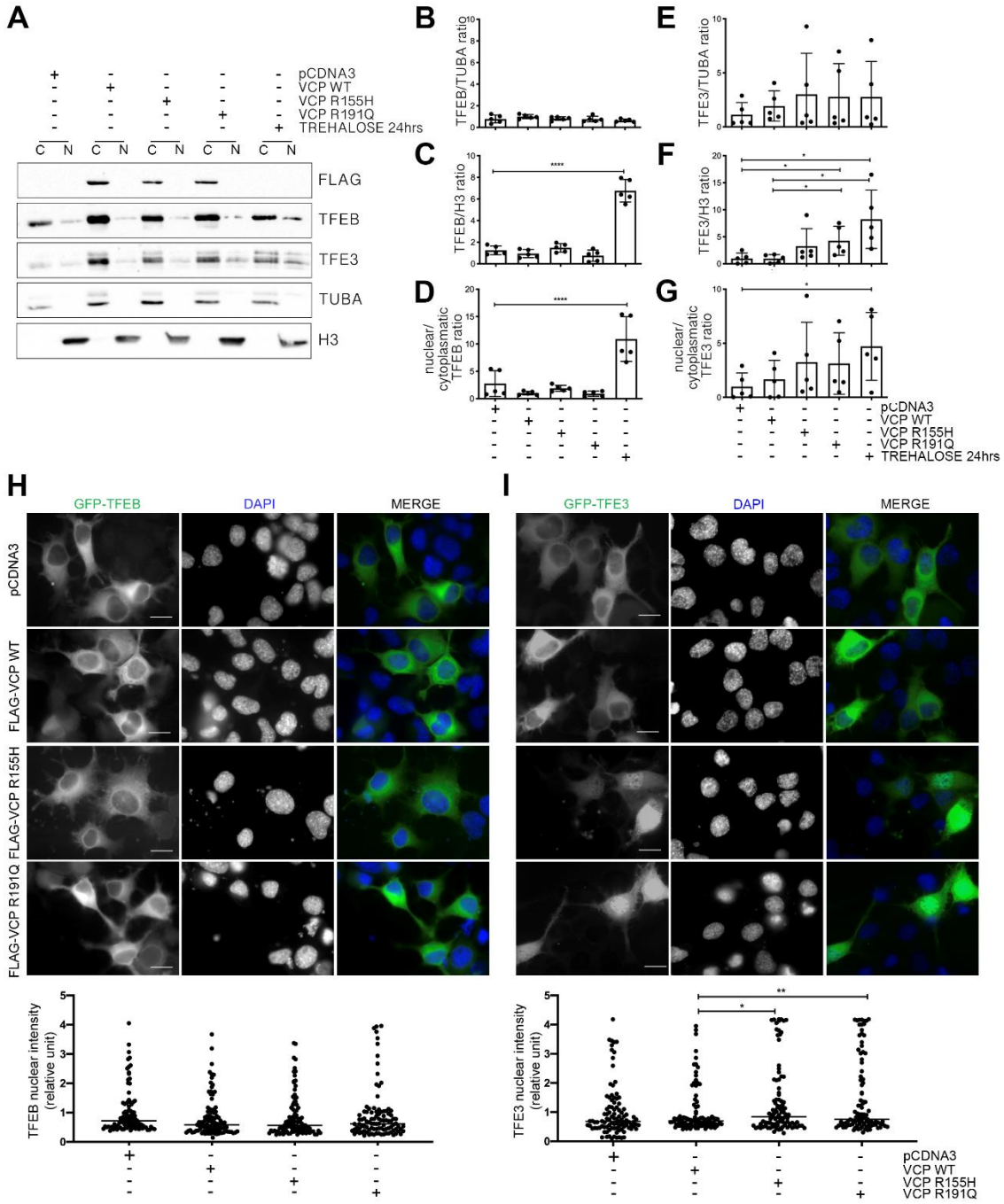

Figure 6. VCP mutants specifically increase TFE3 nuclear levels. (A) A representative WB analysis of cytoplasmic (C) and nuclear (N) extracts of NSC-34 overexpressing WT or mutants FLAG-VCPs. To visualize FLAG-VCP, an anti-FLAG antibody was used. To visualize transcription factors TFEB and TFE3, an anti-TFEB antibody and an anti-TFE3 antibody were used respectively. α-tubulin (TUBA) was used as loading control of the cytoplasmic fraction. Histone 3 (H3) was used as loading control of the nuclear fraction. (B-G) Quantification of WB analysis presented in figure A. (B) The bar graph represents the mean relative optical

density quantification of cytoplasmic fraction of TFEB detected by WB using an anti-TFEB antibody. (C) The bar graph represents mean relative optical density quantification of nuclear TFEB detected by WB using an anti-TFEB antibody. (D) The bar graph represents the ratio of the mean relative optical density quantification of nuclear TFEB and the mean relative optical density quantification of cytoplasmic TFEB detected by WB using an anti-TFEB antibody. (E) The bar graph represents mean relative optical density quantification of cytoplasmic fraction of TFE3 detected by WB using an anti-TFE3 antibody. (F) The bar graph represents mean relative optical density quantification of nuclear TFE3 detected by WB using an anti-TFE3 antibody. (G) The bar graph represents the ratio of the mean relative optical density quantification of nuclear TFE3 and of the mean relative optical density quantification of cytoplasmic TFE3 detected by WB using an anti-TFE3 antibody. All quantification histograms were calculated using the mean ±SD for 5 independent samples (One-way ANOVA followed by Fisher's LSD test and the unpaired t-test with Welch's correction; *$p<0.05$, **$p< 0.01$). (H) Upper inset shows fluorescence microscopy analysis (63x magnification) of NSC-34 overexpressing WT or mutants FLAG-VCPs and GFP-TFEB. TFEB was visualized as GFP-TFEB (green) and nuclei were stained with DAPI (blue). Scale bar, 10 μm. The bar graph (lower inset) represents the quantification of TFEB nuclear intensity; the fields were randomly selected and at least 100 cells were analyzed for each condition (one-way ANOVA with Fisher's LSD test). (I) Upper inset shows fluorescence microscopy analysis (63 x magnification) of NSC-34 overexpressing WT or mutants FLAG-VCPs and GFP-TFE3. TFE3 was visualized as GFP-TFE3 (green) and nuclei were stained with DAPI (blue). Scale bar, 10 μm. The bar graph (lower inset) represents the quantification of TFE3 nuclear intensity; the fields were randomly selected and at least 100 cells were analyzed for each condition (one-way ANOVA with Fisher's LSD test; *$p<0.05$, **$p<0.01$).

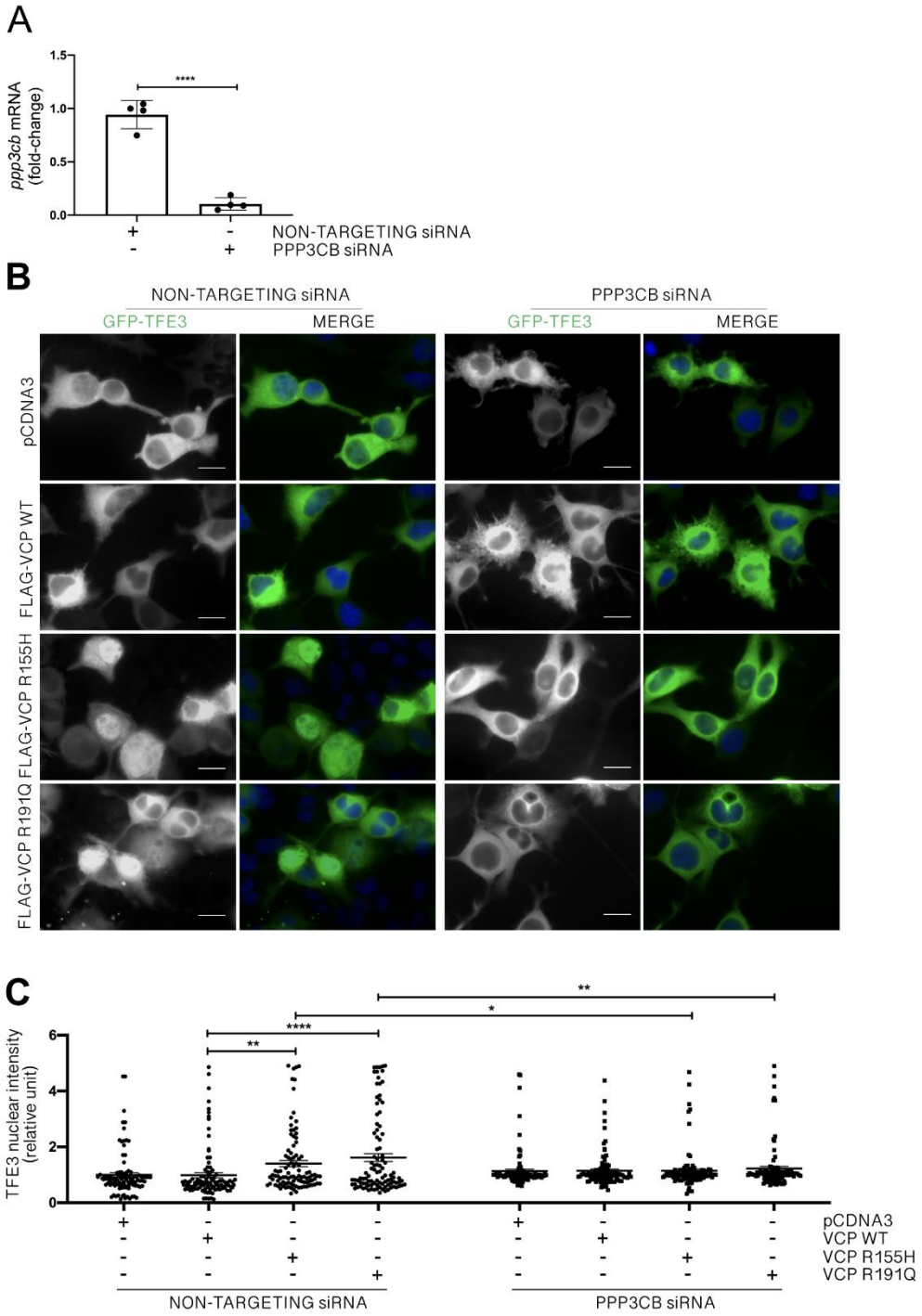

Figure 7. PPP3CB mediates TFE3 translocation induced by VCP mutants. (A) RT-qPCR for PPP3CB mRNA normalized with Rplp0 mRNA levels. Data are means ± SD of 4 independent samples (unpaired student t-test; ****p<0.0001) (B) Fluorescence microscopy analysis (63x magnification) of NSC-34 overexpressing WT or mutants FLAG-VCPs and transfected with PPP3CB or non-targeting siRNAs. TFE3 was visualized as GFP-TFE3 (green), and nuclei were stained with DAPI (blue). Scale bar, 10 μm. (C) The bar graph represents the quantification of

TFE3 nuclear intensity; the fields were randomly selected and at least 100 cells were analyzed for each condition (two-way ANOVA with Fisher's LSD test; *p<0.05, **p< 0.01, ****p<0.0001).

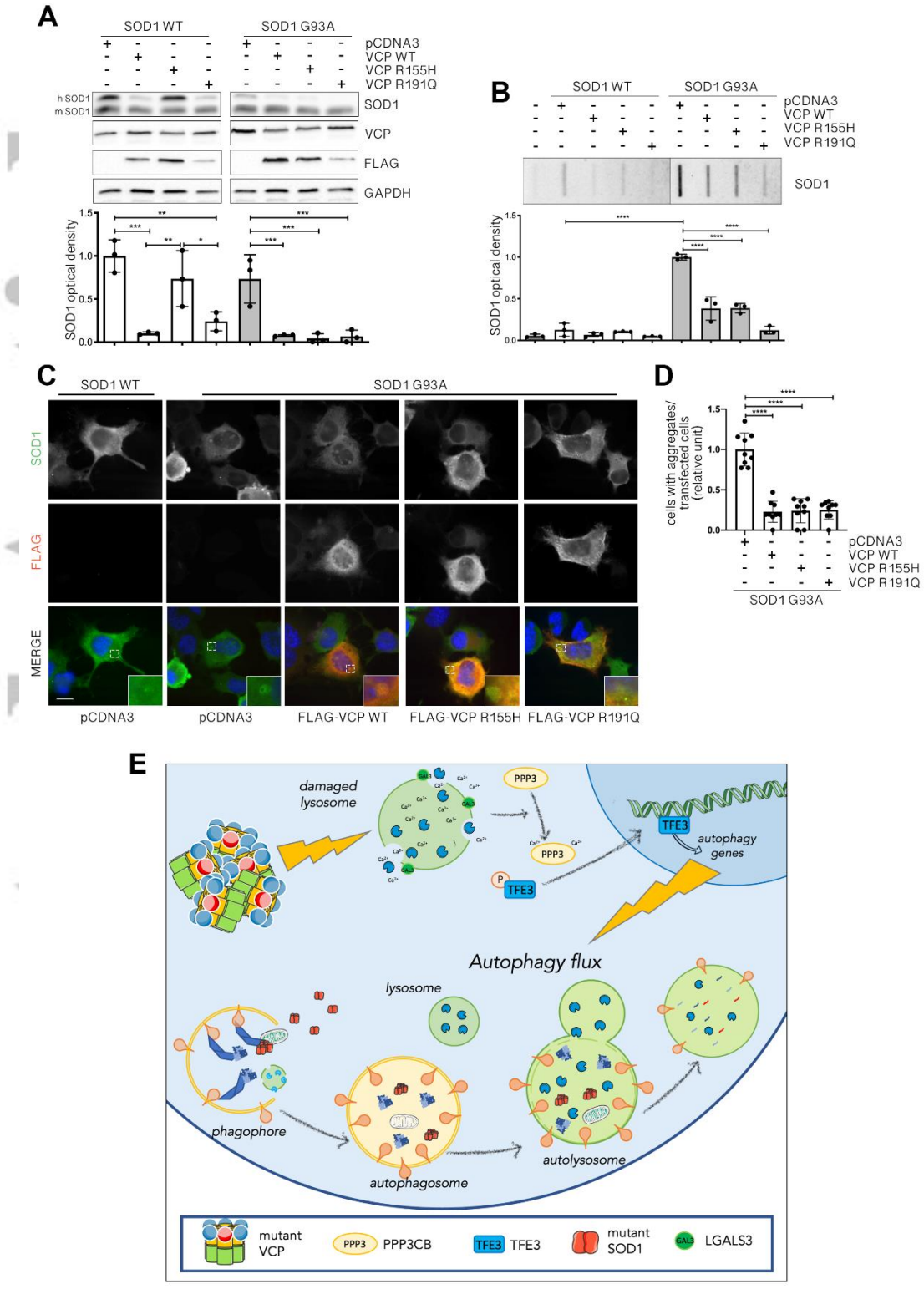

Figure 8. WT and mutants VCPs enhance G93A SOD1 clearance. (A) A representative WB (upper inset) of PBS extracts added with SDS, from NSC-34 cells overexpressing WT SOD1 or G93A SOD1 and WT or mutants FLAG-VCPs. To visualize exogenous human (upper lane) or endogenous murine (lower lane) SOD1, an anti-SOD1 antibody was used. To visualize total

VCP, an anti-VCP antibody was used. To visualize overexpressed FLAG-VCPs, an anti-FLAG antibody was used. GAPDH was used as loading control. The bar graph represents the optical densitometry quantification of SOD1 detected in WB (lower inset) (one-way ANOVA with Fisher's LSD test; *p<0.05, **p<0.01, ***p<0.001). (B) FTA (upper inset) of PBS extracts from NSC-34 cells overexpressing WT or G93A SOD1 and WT or mutants FLAG-VCPs. To visualize SOD1 an anti-SOD1 antibody was used. The bar graph represents the mean relative optical density quantification of FTA (lower inset) (one-way ANOVA with Fisher's LSD test; ****p<0.0001). (C) IF microscopy analysis (63x magnification) on NSC-34 overexpressing WT SOD1 or G93A SOD1 and WT or mutants FLAG-VCPs. SOD1 was stained with an anti-SOD1 antibody (green), FLAG-VCPs were stained with an anti-FLAG antibody (red), and nuclei were stained with DAPI (blue). A 4x magnification of selected areas is shown. Scale bar, 10 μm. (D) The bar graph represents the quantification of the ratio cells with aggregates/transfected cells of NSC-34 transfected WT SOD1 or G93A SOD1 and WT or mutants FLAG-VCPs; the fields were randomly selected and at least 50 cells for each sample were counted over 9 independent biological samples for each condition (n=9) ± SD (One-way ANOVA followed by Fisher's LSD test; ****p<0.0001). (E) Proposed novel pathological mechanism for VCP mutants. Proposed model for the pathological mechanism exerted by VCP mutants in neuronal cells. VCP mutants aggregate and cause lysosomal size and morphology alteration and damage. Lysosomal damage, via PPP3CB, specifically causes TFE3 dephosphorylation and nuclear translocation. Active TFE3 promotes autophagy activation, which results in an increased flux if compared to basal conditions. The increased autophagic flux leads to the clearance of damaged lysosomes via lysophagy and eventually enhances the clearance of misfolded proteins (e.g., mutant SOD1). This figure was created using Servier Medical Art templates, which are licensed under a Creative Commons Attribution 3.0 Unported License; https://smart.servier.com.